FIBER BRAGG GRATING (FBG) SENSORS FOR THE SIMULTANEOUS MEASUREMENTS OF STRAIN AND TEMPERATURE

by

ABHAY KUMAR SINGH

Presented to the Faculty of the Graduate School of

The University of Texas at Arlington in Partial Fulfillment

of the Requirements

for the Degree of

MASTER OF SCIENCE IN MECHANICAL ENGINEERING

THE UNIVERSITY OF TEXAS AT ARLINGTON

December 2016

Acknowledgements

I would like to express my sincere gratitude to my advisor Prof. Haiying Huang for the continuous support throughout my graduate study and research: for her patience, motivation, enthusiasm, and immense knowledge.

Besides my advisor, I would like to thank my thesis committee: Dr. Ankur Jain and Dr. Bo. P. Wang for their encouragement, insightful comments, and support.

My sincere thanks also goes to the program manager Dr. Ignacio Perez, office of Naval research, for his supports, suggestions, and for funding this project.

I thank my fellow labmates in Advance Sensor and Technology Laboratory (ASTL): Franck Tchafa, Kranthi Balusu, and Jalal Fathi Sola for the stimulating discussions, working together before deadlines, and for all the fun we have had.

Finally, I must express my very profound gratitude to my parents for providing me with unfailing support and continuous encouragement throughout my years of study. This accomplishment would not have been possible without them. Thank you.

Nov. 30, 2016

Abstract

This research presents a single fiber Bragg grating (FBG) sensor that is capable of measuring the axial load and temperature simultaneously. The FBG sensor is coated with a block of recrystallized Lophine, which introduces the bandwidth modulation of the FBG reflectance spectrum. Thermal-mechanical testing of the Lophine-coated FBG sensor under different load and temperature combinations was carried out. It was discovered that the FBG bandwidth is linearly proportional to the applied load and temperature. By fitting the measured FBG bandwidths and central Bragg wavelengths as linear functions of the axial load and temperature, we demonstrated that the axial load and temperature can be inversely determined from the measured reflectance spectrum of a single Lophine-coated FBG sensor. The measurement errors for the axial load and the temperature were found to be ±4 gm and ±4 °C, respectively.

Table of Contents

List of Illustrations

Chapter 1

Chapter 2

Introduction

Optical fiber sensors are the sensor of choice for Structural Health Monitoring (SHM), primarily due to their light weight, compact size, inexpensive cost, and immunity to electro-magnetic interference (EMI) etc.[1–3]. Fiber Bragg grating (FBG) based sensors are the most widely accepted optical fiber sensors in the SHM community [4–6]. One of the unique advantages of the FBG sensors is that the FBG is directly inscribed into a conventional optical fiber. As such, the interface between the sensing element (i.e. the FBG section) and the optical fiber for signal transmission is seamless. Incorporating FBG sensors in an optical fiber therefore does not require labor intensive integration and does not compromise the mechanical strength or compactness of the optical fiber. In addition, the physical measurands are extracted from the spectral parameter of the FBG, which renders the measurements more reliable, more robust, and more sensitive to minute changes. An added advantage of this wavelength encoded sensing mechanism is that the sensor is self-referencing and can provide absolute measurements. Maybe one of the most attractive features of the FBG sensors is their capability to be multiplexed in the wavelength domain. Since the reflectance spectrum of an FBG has a very narrow bandwidth of a fraction of nanometers, multiple FBG sensors can be implemented in a single strand of optical fiber based on the principle of wavelength division multiplexing. This unique feature enables deploying a large number of sensors without incurring substantial cost or weight penalties.

Challenges

One of the long standing challenges of the FBG based sensors is their cross-sensitivity to strain and temperature [7,8]. Strain is one of the most important physical parameters that can reveal a structure's loading, boundary, fatigue, and material conditions. Strain measurement, therefore, is an indispensable capability for any SHM system. When bonded on a structure, an FBG sensor is expected to experience the same strain as the host structure. Since the Bragging wavelength, λ_B, is related to the effective refractive index (R.I.) of the core mode n_{eff} and the fiber grating period Λ as:

$$\lambda_B = 2n_{eff}\Lambda\,. \tag{1-1}$$

The sensitivity of the Bragging wavelength λ_B to the applied strain ε can be derived by taking the total derivative of equation 1-1 with respect to the applied strain ε, i.e.

$$\frac{d\lambda_B}{d\varepsilon} = 2\Lambda\frac{\partial n_{eff}}{\partial\varepsilon} + 2n_{eff}\frac{\partial\Lambda}{\partial\varepsilon} = \lambda_B\left(\frac{1}{n_{eff}}\frac{\partial n_{eff}}{\partial\varepsilon} + \frac{1}{\Lambda}\frac{\partial\Lambda}{\partial\varepsilon}\right) \approx \lambda_B(\alpha_\varepsilon + 1)\,, \tag{1-2}$$

in which α_ε represents the photo-elastic constant of the optical fiber. The strain sensitivity for a typical FBG strain sensor is 1.2 pm $\mu\varepsilon^{-1}$ [9] which means 1000 $\mu\varepsilon$ will shift the Bragging wavelength by 1.2 nm. Unfortunately, temperature variations have similar effects on the Bragging wavelength. The temperature sensitivity of the Bragging wavelength λ_B can be derived following the same procedure, which results in

$$\frac{d\lambda_B}{dT} = 2\Lambda\frac{\partial n_{eff}}{\partial T} + 2n_{eff}\frac{\partial\Lambda}{\partial T} = \lambda_B\left(\frac{1}{n_{eff}}\frac{\partial n_{eff}}{\partial T} + \frac{1}{\Lambda}\frac{\partial\Lambda}{\partial T}\right) = \lambda_B(\alpha_n + \alpha_T)\,, \tag{1-3}$$

where α_n is the thermo-optical constant of the fiber and α_T is the thermal expansion coefficient of the fiber material. The temperature induced FBG wavelength shift is typically 13 pm °C^{-1}, i.e. every 1 °C change in temperature will cause the Bragg wavelength λ_B to shift by 13 pm [9]. Without any temperature compensation, a 5 °C temperature changes would then result in a misreading of the applied strain by 55 $\mu\varepsilon$. Due to this cross-sensitivity

to strain and temperature, it is critical to differentiate the effects of strain and temperature on the FBG wavelength shifts.

Current Research Efforts and Limitations

Many techniques have been developed to address the cross-sensitivity limitation of the FBG sensors [5]. The most common approach is to implement two FBG sensors with one bonded on the structure and the other being free standing[10]. Because the free standing FBG sensor is not subjected to strain, it can be used for temperature sensing solely. The strain experienced by the bonded FBG sensor can then be inferred from the wavelength shift once the temperature is known. Ensuring the free-standing FBG sensor to satisfy the strain-free condition, however, requires special packaging techniques [10]. Other researchers addressed the FBG cross-sensitivity problem by combining one FBG sensor with a sensor of different types, such as an extrinsic Fabry-Perot interferometer [11], a long period fiber grating [12,13], an etched FBG [14] etc. Adding the reference sensor, in general, increases the sensor length and thus reduces the spatial resolution. In addition, the sensor pair has to be placed in close vicinity to minimize the errors introduced by the strain and temperature gradients. Combining FBGs with specially doped fibers has also been studied to differentiate the temperature and strain effects [15,16]. Specialty fibers, on the other hand, are much more expensive than conventional fibers and thus could increase the system costs substantially. Besides, the specialty fibers have to be spliced with conventional communication fibers, which may not be a trivial task.

Techniques using one single FBG sensor for temperature-compensated strain measurement have also been investigated. One common scheme is to package the FBG sensors on specially designed structures that introduce uneven deformation of the FBG sensors when the ambient temperature changes. Structures such as a cantilever beam

[17], a polymer taper [18], a bilateral cantilever beam [19] etc. have been studied. The disadvantage of such methods is that the packaging makes the FBG sensor quite bulky, which offsets the compact and light weight features of the optical fiber sensors. Recently, superstructured FBGs have been exploited to minimize the strain-temperature cross-sensitivity of the FBG sensors [8,20,21]. A superstructured FBG is essentially the superposition of an FBG and a long period grating induced by micro-bending. The superstructure (i.e. the long period grating) generates additional spectral peaks (i.e. side bands) in the reflectance spectrum of the FBG sensor. The reflectivity of the side bands increases with strain but reduces with temperature. Combining the side band reflectivity with the FBG wavelength shift therefore enables simultaneous measurement of strain and temperature. A major disadvantage of this approach is that the wavelength allocation of each FBG sensor has to be increased due to the side bands introduced by the superstructure. As a result, the number of FBG sensors that can be accommodated within a given wavelength band has to be reduced.

Compared to the Bragg wavelength, the bandwidth of the FBG reflectance spectrum has received very little attention as a measurement parameter for FBG sensor interrogation. Even though researchers have long observed that embedding FBGs in composite materials may broaden the FBG spectrum and this effect is temperature dependent [4,22], this phenomenon is considered as a limitation of the FBG sensors that need to be minimized instead of exploiting it for sensing purpose. One exception is the temperature compensated strain sensor presented by [23]. By embedding an FBG sensor in epoxy and sandwiching it with composite laminates, they attempted using the FBG bandwidth to compensate for temperature. However, they only obtained consistent temperature sensitivity using Apodized FBGs. In addition, the measurement errors are around 900 $\mu\varepsilon$. Considering that the strain and temperature sensitivity of a typical FBG is

1.2 pm $\mu\varepsilon^{-1}$ and 13 pm °C^{-1} respectively [9], a measurement error of 900 $\mu\varepsilon$ is equivalent to a temperature variation of 83 °C, which is substantially higher than the temperature fluctuation a structural component normally experiences. Besides embedding the FBG sensor in composites, the bandwidth of an FBG sensor can also be broadened by subjecting the FBG sensor to non-uniform displacements, such as bonding it to a beam structure [21,24] or embedding it in composite laminates [25]. These sensors, however, are rather bulky and thus are only suitable for temperature-compensated displacement measurement. Chirped FBGs, which has a broader bandwidth as compared to uniform FBGs, were studied for temperature-independent strain sensing [26,27]. In both work, the broadening of the FBG reflectance spectrum was measured as the power of the light reflected by the chirped FBG. As such, only the strain information can be inferred from the power measurement.

Proposed Technique

Addressing the long-standing limitation of FBG sensors (i.e. their cross-sensitivity to strain and temperature): Almost all of the FBG sensors developed so far rely on one spectral parameter, i.e. the Bragging wavelength, to deduce the sensing parameter. Since the Bragging wavelength is sensitive to both strain and temperature changes, decoupling the effects of strain and temperature on the Bragging wavelength has been an active research in the past couple of decades. Despite of the intensity researches carried out in the past, simultaneous strain and temperature measurement using a single FBG has not been achieved. We believe this research is the first attempt in introducing the spectral bandwidth of the FBG as a spectral parameter in addition to the Bragg wavelength.

Thesis Objective

The objective of this research is to demonstrate simultaneous strain and temperature measurement using a single Fiber Bragg Grating (FBG) sensor. The research hypothesis is that the bandwidth of an FBG spectrum can be modulated as a function of temperature. This could be achieved through either of the three methods:

(1) An FBG can be designed so that its spectral bandwidth is related to the optical absorption of the coating material. Adopting a thermochromic coating with a temperature-dependent absorption, therefore, will cause the FBG spectral bandwidth to change with temperature.

(2) The presence of externally induced birefringence in an FBG can also modulate bandwidth. Embedding an FBG into a composite laminates distorts the orthogonal symmetry of the fiber and polarizes the light, which in turn, splits the unique Bragg condition and introduces thermal dependent bandwidth change.

(3) When an FBG is exposed to an un-even thermal residual stress, bandwidth of the FBG spectrum broadens which in turn is a function of temperature change.

The proposed sensor is based on modulating both the spectral parameters of an FBG spectrum, i.e. Bragg wavelength and bandwidth. By combining the shift in Bragg wavelength of the FBG spectrum along with the change in its bandwidth we should be able to measure temperature and strain at the same time and thus solve the problem of cross sensitivity associated with them.

Chapter 3

Background

Fiber structure and Physics

Optical fiber is a circular wave-guide that is used to transport signal in the form of light. As shown in figure 2-1, it consists of two concentric cylinders. The inner cylindrical region is called core and it has slightly higher index of refraction. The outer region is called cladding and its index of refraction is slightly lower (by ≈ 1%) than the core. In general, optical fibers are made of silica in which index-modifying dopants, such as GeO_2, are added. A protective coating of acrylate is provided at the top of the cladding region, as shown in figure 2-1, to reduce signal loss that occurs when fibers are pressed against rough surfaces. For environmental protection, fibers are incorporated into cables by providing a polyethylene sheath that encases the fiber within a strength member such as steel or Kevlar strands.

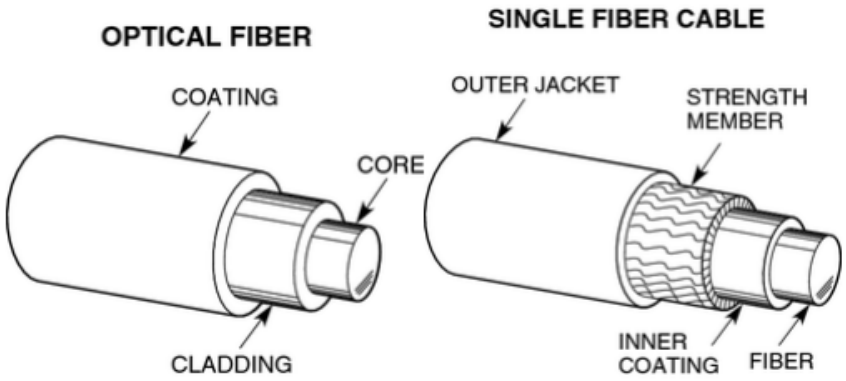

Figure 3-1 Cross section view of optical fiber and single fiber cable [48].

Since the core has a higher index (n_1) of refraction than the cladding (n_2), light can be guided in the core following Snell's law. A typical ray diagram of light propagation in the optical fiber is shown in the figure 2-2. Before light enters the fiber, it goes under refraction

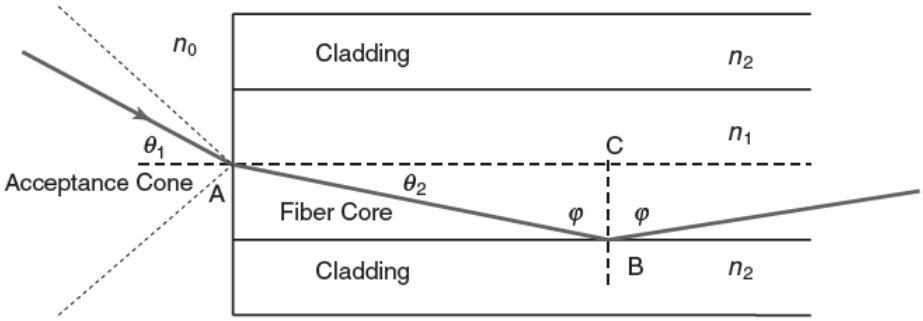

Figure 3-2 Propagation of light in optical fiber [28].

at the interface between fiber and external medium (let's say air, n_0). This refracted ray acts as an incident ray for the light travelling in the fiber and controls its angle of incidence. In order to satisfy the criteria of total internal reflection (TIR) for the light travelling in the fiber, the angle of incident ray (ϕ) should be greater than the critical angle. This angle can be related to the angle of acceptance (θ_1) using snell's law and is shown by equation 2-1. The angle of acceptance is simply defined as the maximum angle of incidence (θ_{acc} = max θ_1) at air-fiber interface that allows TIR of the light travelling in the fiber and the sine function of the acceptance angle is referred to the *numerical aperture (NA),* shown in equation 2-2.

$$n_0 \sin\theta_1 = n_1 \sin\theta_2 \ , \tag{2-1}$$

$$NA = n_0 \sin\theta_1 = \sqrt{{n_1}^2 - {n_2}^2} \ , \tag{2-2}$$

where n_0, n_1 and n_2 are the refraction indexes of air, fiber core and cladding, respectively.

In fiber, light travels in two different modes: radiation modes and guided modes. In radiation modes, energy is coupled out of the core and is quickly dissipated. However guided modes are confined to the core, and propagate along the fiber, transporting information and power. For a large fiber core, many simultaneous guided modes can be supported, each having its own distinct velocity and can be further decomposed into orthogonal linearly polarized components.

Classification of Optical Fiber

Optical fiber is mainly classified on the basis of number of modes of the propagating signal that a fiber can support, which in turn, depends on the numerical aperture of the fiber, its core diameter and the wavelength of the guided wave. In general, there are two types of optical fiber as follows:

1) Single-mode fiber (SMF) and
2) Multi-mode fiber (MMF).

Often normalized frequency parameter (also known as V-number), as shown in equation 2-3, is used to determine if the fiber is SMF or MMF. As long as the value of V-number is less than 2.405, there would be a single mode travelling in the fiber and the fiber would be characterized as SMF [28]. However, for a V-number greater than 2.405, fiber behaves as a MMF.

$$V = \frac{2\pi a}{\lambda} NA\,, \tag{2-3}$$

where λ is the wavelength of guided wavelength and '*a'* is the core radius.

Single-mode fiber (SMF):

An optical fiber having the V-number less than 2.405 is called SMF. It restrict the transmission signal only to a single mode. The typical core diameter of SMF fiber lies between 8-10 *μm* and cladding diameter is 125 *μm*. Fiber, in its simplest form, has a step index profile with an abrupt boundary separating a high index core and a lower index cladding. For most of the fiber, the refractive index differential is 0.36% and is well under 1% in other standard types. Figure 2-3 shows the cross section of two principle types of step index SMF made from fused silica. The simplest design is the matched-cladding fiber shown in figure 2-3(a). An alternate design is the depressed cladding fiber shown in the figure 2-3(b).

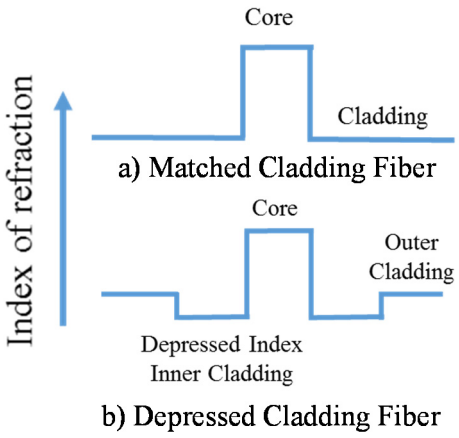

Figure 3-3 Two types of step index SMF; (a) Matched cladding fiber and (b) Depressed cladding fiber.

Multi-mode fiber (MMF):

A multimode fiber can support the propagation of a number of modes (rays) as long as V-number is greater than 2.405. These fibers are characterized by a large core diameter (50 or 62.5 microns). The MMF can either have a step index profile with an abrupt boundary separating a high index core and a lower index cladding or can have a graded index fiber, as shown in figure 2-4. In the graded-index fiber the refractive index changes

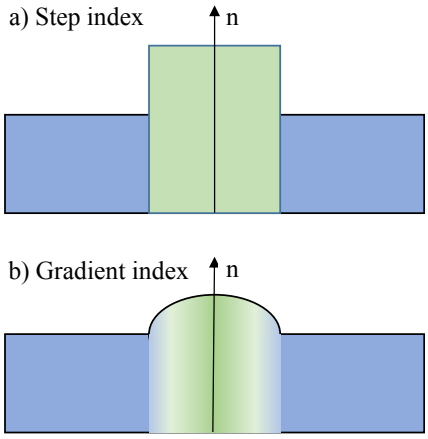

Figure 3-4 Two types of MMF; (a) Step index and (b) Gradient index.

progressively from the core to the cladding. The refractive index of the core is the highest in the center of the core and gradually decreases approaching the core-cladding interface.

Bragg Grating

FBG is a longitudinal periodic or semi-periodic variation of the index of refraction in the core of an optical fiber [29]. These types of uniform fiber gratings, where the phase fronts are perpendicular to the fiber longitudinal axis and the grating planes are of a constant period (figure 2-5), are considered the fundamental building blocks for most Bragg grating structures. Light guided along the core of an optical fiber will be scattered by each grating plane. If the Bragg condition is not satisfied, the reflected light from each of the subsequent planes becomes progressively out of phase and will eventually cancel out. Where the Bragg condition is satisfied, the contributions of reflected light from each grating plane add constructively in the backward direction to form a back-reflected peak with a center wavelength defined by the grating parameters. The Bragg grating condition is simply the requirement that satisfies both energy and momentum conservation. Energy

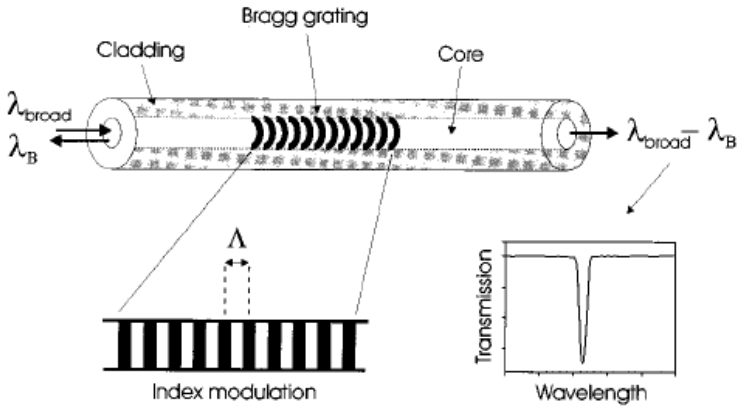

Figure 3-5 Schematic of fiber Bragg grating with uniform index-modulation, amplitude and period [29].

conservation requires that the frequency of the incident radiation and the reflected radiation is the same. Momentum conservation requires that the incident wave vector, k_i, plus the grating wave vector, K, equal the wave vector of the scattered radiation k_f, this is simply stated as:

$$K_i + K = K_f, \tag{2-4}$$

where the grating wave vector, K, has a direction normal to the grating planes and it has a magnitude 2Π/Λ, (Λ is the grating spacing shown in figure 2-5). The diffracted wave vector is equal in magnitude but opposite in direction to the incident wave vector. Hence, the momentum conservation condition becomes,

$$2\,\frac{2\,\pi\,n}{\lambda_B} = \frac{2\,\pi}{\Lambda}, \tag{2-5}$$

which simplifies to the first-order Bragg condition

$$\lambda_B = 2\,n\,\Lambda\,, \tag{2-6}$$

where the Bragg grating wavelength, λ_B , is the free-space center wavelength of the input light that will be back reflected from the Bragg grating, and *n* is the effective refractive index of the fiber core at the free-space-center wavelength.

Types of Fiber Bragg Gratings

There are several distinct types of fiber Bragg grating structures such as the common Bragg reflector, the blazed Bragg grating, and the chirped Bragg grating [29]. These fiber Bragg gratings are distinguished either by their grating pitch (spacing between grating planes) or tilt (angle between grating planes and fiber axis). The most common fiber Bragg grating is the Bragg reflector, which has a constant pitch. The blazed grating has phase fronts tilted with respect to the fiber axis, that is, the angle between the grating planes and the fiber axis is less than 90°. The chirped grating has an aperiodic pitch, that is, a monotonic increase in the spacing between grating planes.

Common Bragg Grating

The common Bragg grating is the simplest and most used fiber Bragg grating as shown in the figures 2-5. Depending on the parameters such as grating length and magnitude of induced index change, the Bragg reflector can function as a narrow-band transmission or reflection filter or a broadband mirror. In combination with other Bragg reflectors, these devices can be arranged to function as bandpass filters.

Blazed Bragg Grating

Tilting (or blazing) the Bragg grating planes at angles to the fiber axis (figure 2-6) will result in light that is otherwise guided in the fiber, to be coupled out of the fiber core into loosely bound guided cladding modes or into radiation modes outside the fiber. The tilt of the grating planes and strength of the index modulation determines the coupling efficiency and bandwidth of the light that is tapped out.

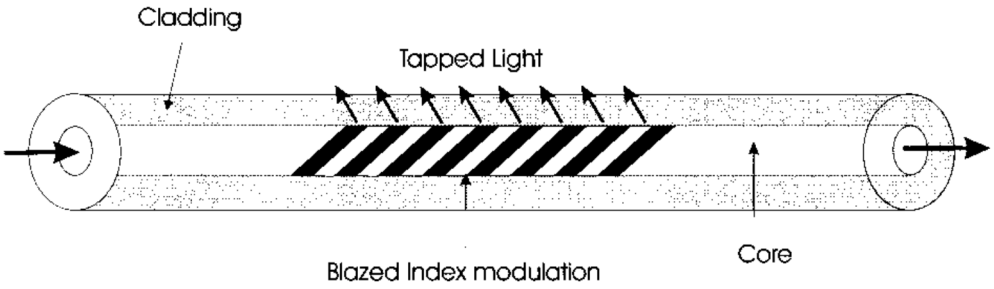

Figure 3-6 Schematic of light coupling between core and cladding of a blazed fiber Bragg grating [29].

Chirped Bragg Grating

A chirped Bragg grating is a grating that has a monotonically varying grating period, figure 2-7. This can be realized by axially varying either the period of the grating Λ or the index of refraction of the core or both.

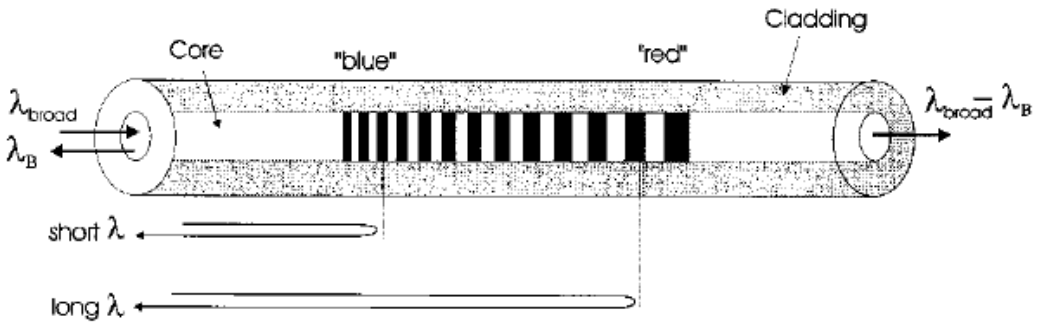

Figure 3-7 Schematic diagram of a chirped grating with a non-periodic pitch [29].

Apodized Bragg Grating

When the profile of the index modulation along the fiber length is given a bell-like functional shape, it is called Apodized Bragg grating and is shown in figure 2-8. It is important in the applications to lower or eliminated the reflectivity of the side-lobes and to get sharp spectral responses.

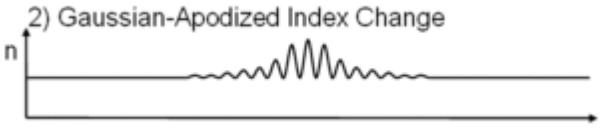

Figure 3-8 Apodized Bragg grating (source: Internet).

Chapter 4

Principle of Operation

An FBG spectrum is characterized by two important parameters, i.e. Bragg wavelength and bandwidth. Bragg wavelength is very popular and has been continuously exploited by the researchers to determine the physical quantities. However, the bandwidth of the FBG reflectance spectrum has received very little attention as a measurement parameter for FBG sensor interrogation. Even though researchers have long observed that embedding FBGs in composite materials may broaden the FBG spectrum and this effect is temperature dependent [4,22], this phenomenon is considered as a limitation of the FBG sensors that need to be minimized instead of exploiting it for sensing purpose. However, our research approach is focused on exploiting all those means to modulate the bandwidth of the reflected FBG spectrum and combine it with Bragg wavelength shift to measure simultaneous change in temperature and strain. Based on the previous research [22,30,31], we know that there are three different ways one can introduce bandwidth change in the FBG spectrum:

(1) Optical absorption of the light interacting with a material of changing absorptivity;
(2) Externally induced variable birefringence;
(3) Due to un-even thermal residual stress.

Among these three approaches of the bandwidth modulation, we adopted the method of optical absorption for the development of our sensor. The other two methods are presented in detail in chapter 6. The proposed optical fiber sensor is shown in figure 3-1. The sensor is an FBG coated with a thermochromic material (figure 3-1(a)). The purpose of the thermochromic coating is to introduce the temperature dependent absorption of the

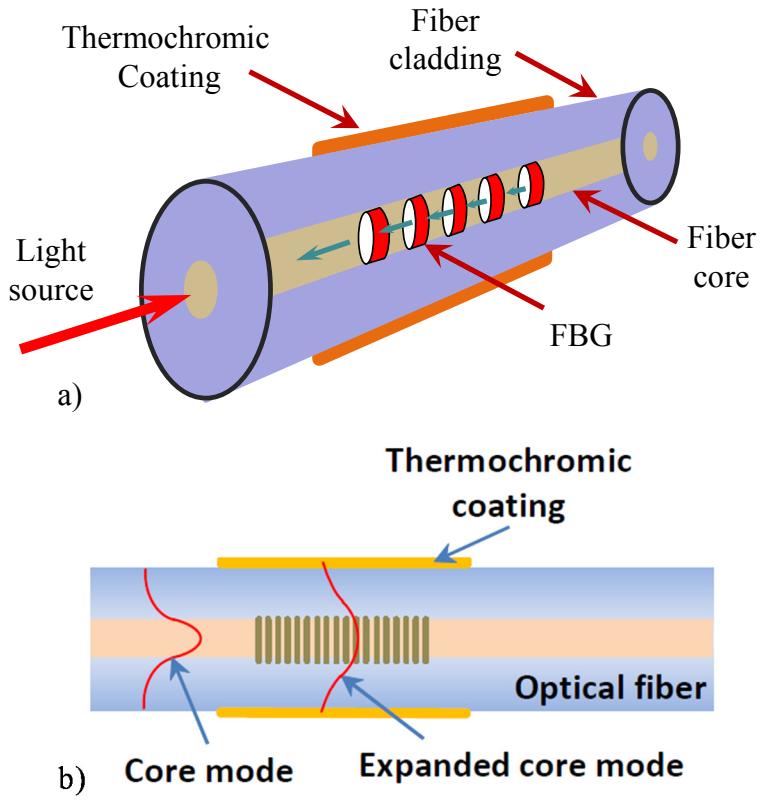

Figure 4-1 Schematic of the proposed strain - temperature sensor; a) configuration of the sensor; b) an FBG with an enlarged core mode.

guided modes supported by the optical fiber, which in turn causes the spectral bandwidth of the FBG to vary with temperature [30]. To improve the interaction between the guided modes and the thermochromic coating the mode profile of the core mode is expanded, as shown in figure 3-1(b). As such, the evanescent field of the core mode can interact with the thermochromic coating. Combining the spectral bandwidth with the FBG wavelength shift will enable us to extract the strain and temperature information simultaneously using a single FBG.

Effect of coating absorption on FBG spectrum

The effect of the coating material on the bandwidth of the FBG resonances was studied by [30]. Several strong Bragg gratings were written in different fibers that exhibit the coupling of the forward propagating LP_{01} core mode to the backward propagating cladding modes. The cladding mode attenuation was easily achieved by depositing a thin lossy layer on the cladding surface. As shown in figure 3-2, the bandwidth of the core-cladding coupling resonance increased steadily with the optical absorption of the coating material. Correspondingly, the transmission losses also increased with the bandwidth broadening but the spectral location of the resonances remained the same. In our case, the resonant bandwidth will be controlled by the absorption of the thermochromic material. As long as the optical absorption of the thermochromic material is monotonously related to the temperature variations, we should be able to extract the temperature information from the resonant bandwidth changes.

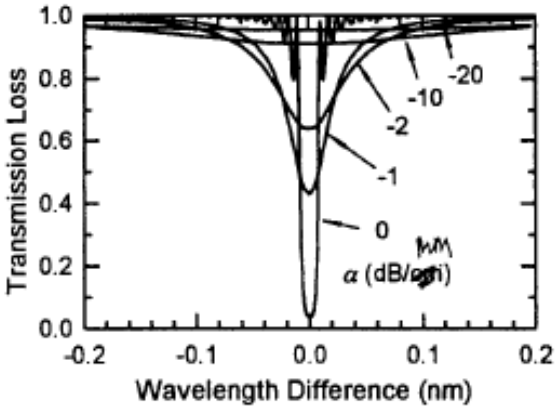

Figure 4-2 Spectral bandwidth increase of a cladding mode resonance as the absorption of the coating material increases [30].

Thermochromic materials for optical absorption

A thermochromic material changes its spectral absorbance with temperature variations [32]. The most common thermochromic materials include luco dyes, liquid crystals, and metal oxides. Recently, thermochromic materials that can operate at the near-infrared (NIR) wavelengths have been under intensive researches due to their potential to achieve energy efficient windows that can reflect more infrared solar energy as temperature rises [33,34]. Vanadium dioxide (VO_2) is one of the most widely researched thermochromic materials studied for this purpose [32,35]. As shown in figure 3-3, the transmission of a pure VO_2 film reduces steadily with temperature for wavelengths above 1000 nm. At 1550 nm, the transmission decreased from around 65% to around 40% as the temperature was increased from 30 °C to 90 °C. The transmission spectrum can be tuned in a large range by changing the particle size and/or by adding a layer of titanium oxide (TiO_2) on the nanoparticles [35]. Taking these advantages into account, VO_2 can also be used as thermochromic.

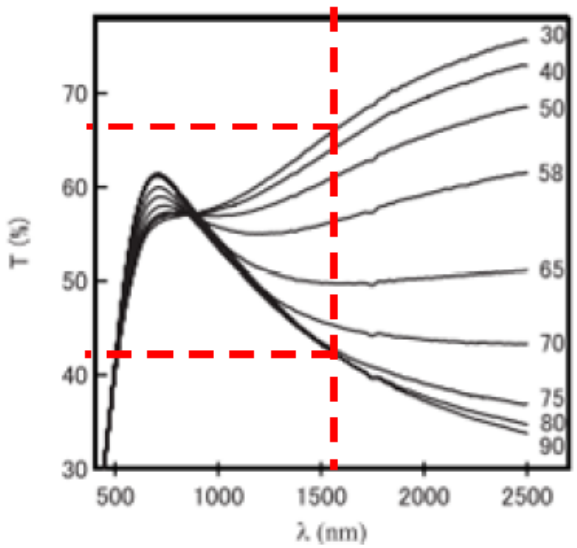

Figure 4-3 Temperature-dependent transmission spectrum of a pure vanadium dioxide (VO_2) film [35].

One thermochromic material that has been studied for optical fiber temperature sensors is lophine [36–38]. As shown in figure 3-4(a), lophine has a relatively constant absorption over a wide wavelength range under a given temperature. The absorption, on the other hand, decreases steadily with temperature increases. At 1310 and 1550 nm, the decrease of the absorption with temperature is pretty linear, as shown in figure 3-4(b). For about 80 °C of temperature change, the absorption of lophine decreased by about 75% (0.4 vs. 1.5). This rate of change is much higher than the sensitivity of the R.I. or the thermal expansion of the fiber, which is in the order of 10^{-5}/°C [9]. Both melted lophine [37] and lophine powder mixed with an epoxy resin [39] were used for fabricating the optical fiber temperature sensors. The lophine based optical fiber temperature sensors, however, have very different configurations from the proposed strain and temperature sensors. Lophine was either directly deposited on a tapered optic fiber [37] or was coated at the distal end of the fiber [36,38,39]. Even though lophine was combined with an FBG for simultaneous strain and temperature [36], it was deposited at the distal end of the fiber instead of functioning as a coating material for the FBG. In addition, all of the aforementioned temperature sensors infer the temperature information directly from the light intensity

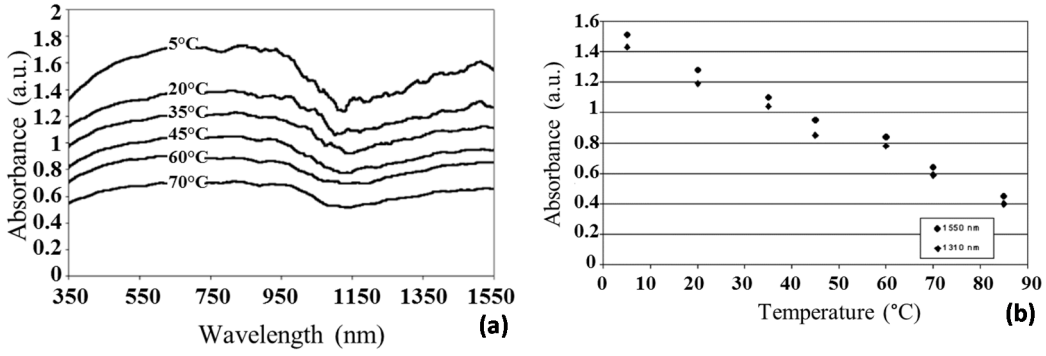

Figure 4-4 Absorbance of Lophine as a function of temperature (a) from 350 nm to 1550 nm and (b) at 1310 and 1550 nm [38].

instead of the spectral bandwidth. Since the light intensity can be easily influenced by the laser power fluctuation and fiber bending losses, intensity based sensing is less reliable and less precise than the sensing mechanisms based on the spectral parameters. To the best of our knowledge, coating an FBG with a thermochromic material for simultaneous strain and temperature measurements has not been reported in the past. In our research, we have used Lophine (2,4,5-Triphenylimidazole) as the thermochromic coating for the bandwidth modulation of the proposed sensor.

Chapter 5

Sensor Fabrication

Grating inscription

FBGs were inscribed in a step index single-mode photosensitive fiber (corning, NA = 0.28) using scanning beam technique [40], as shown in figure 4-1. The fabrication process included a 193 nm excimer laser (Bragg Star Industrial-LN 1000 FT) and a phase mask (1071.5 nm). The grating was written at a uniform scanning speed of 0.37 mm/sec while the laser power was controlled at 5 *mJ* with a repetition of 800 Hz. The phase mask was set at 0 degree tilt angle for straight FBG whereas 4 degree angle was set for Tilted FBG (TFBG) and the grating was written in the length of 6.35 mm (0.25 inch). The entire grating was fabricated by a different lab in collaboration with our project.

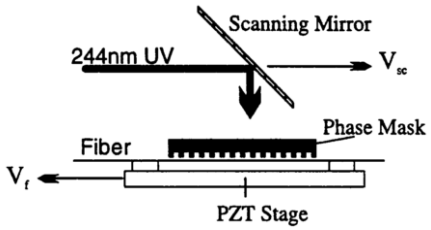

Figure 5-1. Inscribing Bragg gratings in the core of a photosensitive fiber [40].

Coating Process

The proposed sensor design consists of a coating of a thermochromic material developed around grating region of the SMF. In our experiments, we have selected 2,4,5-triphenylimidazole (Lophine) as a transducing element for the sensor. Apart from its thermochromic property, Lophine is a nontoxic hydrophobic material (immune to water molecules) with the melting point at 275–277 °C and is also available at a low cost. In subsequent experiments, we have also used two different non-thermochromic coating materials (Solder paste and NOA-61 epoxy) for validating the results obtained from Lophine coating. The individual coating processes are explained below.

Lophine:

The commercial Lophine comes in the powder form which needs proper adhesive to be used for coating. In our initial approaches we used different solvents and epoxies, such as THF, PVC, NOA-61, NOA-81 etc., to mix Lophine and apply uniformly over FBGs but all the efforts were failed. The major challenge was that the Lophine appeared to change the curing property of the epoxy and was also very little soluble in the solvents used. This motivated us to fuse the Lophine and use its molten form for coating. A similar method was also adopted by [37].

Although it is a challenging task to work with Lophine, especially when it has negligible wettability for glass fiber but having a low melting point of 275–277 °C, it enables us to coat, un-coat and re-coat the FBGs so that the repeatability of the sensor response can be evaluated. In addition, it is very easy to machine the sample and control the height of the coating. In order to coat the FBG sensors with molten Lophine and to control the coating thickness, a mold was designed. As shown in figure 4-2(a), the mold consists of a base plate and two vertical plates. The distance between the two vertical plates was controlled by inserting spacers with the desired thickness. Once the mold was adjusted properly, an optical fiber was placed at equal distances from the vertical plates with the help of a microscope and taped in position using high temperature tapes. To melt the Lophine, a beaker was heated up to 475 °C using a hot plate and Lophine powder was added slowly to the heated beaker (see figure 4-2(b)). Once sufficient molten Lophine was obtained, the molten Lophine was poured carefully into the space between the two vertical plates of the mold. As it cools down, the molten Lophine formed a recrystallized Lophine block with the FBG encapsulated inside, as shown in figure 4-2(c). The Lophine block removed from the mold is shown in Figure 4-2(d), which has rough edges and the optical

fiber is not centered. To smoothen the edge and produce a Lophine block with the optical fiber in the center, the edges of the block were brought in contact with a heated metal plate to remove any excessive Lophine (see figure 4-2(e)). As shown in figure 4-2(f), the FBG sensor is located at the center of a Lophine block with a uniform thickness of 1.5 mm, a height of 3.46 mm, and a length of 46 mm.

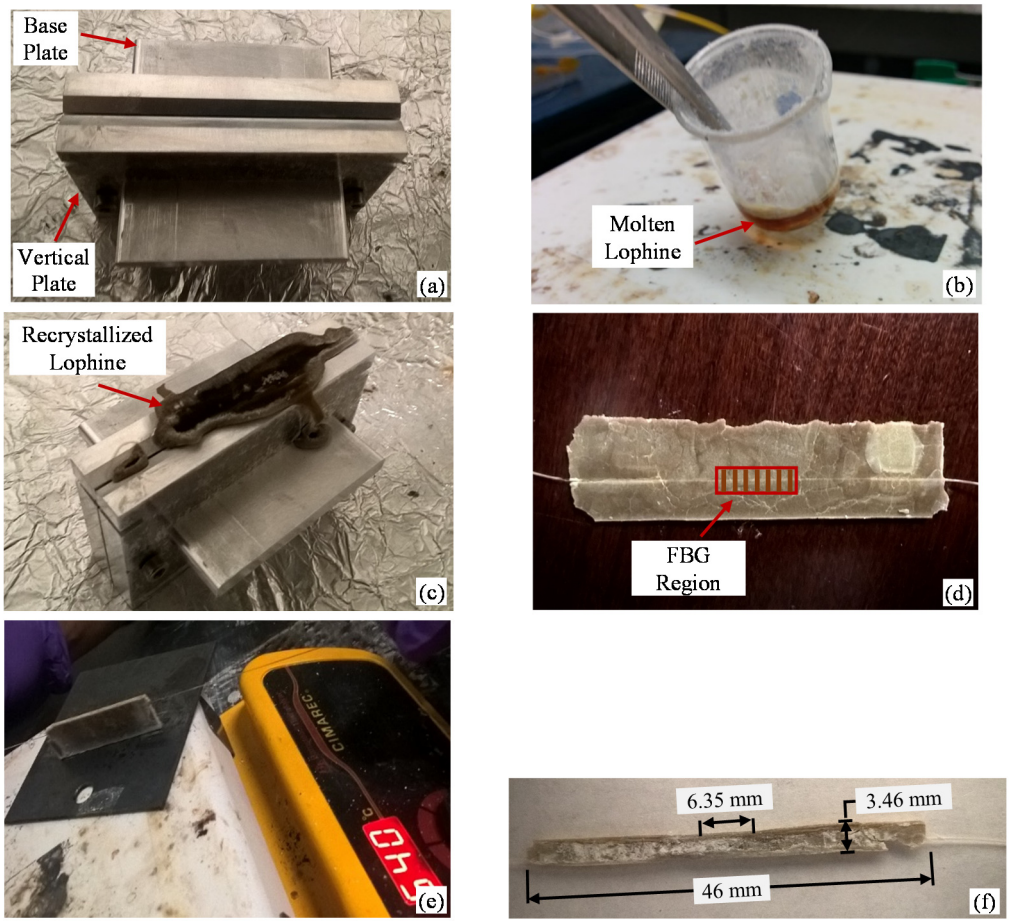

Figure 5-2. Coating Fiber Bragg Grating with recrystallized Lophine: (a) mold for thickness control; (b) melt Lophine in a beaker using a hot plate; (c) recrystallize Lophine in the mold; (d) recrystallized Lophine block with FBG encapsulated inside; (e) reduce the height of the recrystallized Lophine block using a heated plate; (f) final Lophine – coated FBG sample.

Solder Paste:

One of the non-thermochromic coating materials used to validate the result was a solder paste. It was coated at the top of FBG sensor using a soldering gun shown in the figure 4-3(a). A glass slide was used as a base and the FBG was mounted at a distance of 1 mm from it. The solder paste was applied uniformly around the grating length of the SMF and the soldering gun was moved at its top, with uniform speed, while its temperature was maintained at 310°C. Once the paste was melted and then solidified, it was left to cool. The coated block of solder paste is shown in figure 4-3(b).

Figure 5-3. a) Solder gun used for coating process; b) FBG sensor coated with solder paste.

NOA-61:

NOA-61 is a UV curable optical epoxy and does not contain any thermochromic property. To apply its coating on FBG, a glass slide was first covered with a layer of Kapton tape after which fiber was mounted at a height of 1 mm form the base. Then a layer of NOA-61 epoxy was applied along the length of FBG which was then cured with UV radiation for 1 hour (4 watt). The coating thus developed is shown in the figure 4-4.

Figure 5-4. FBG sensor coated with NOA-61 epoxy.

Chapter 6

Characterization of FBG sensor

Experimental Set-up

The response of the FBG sensors were recorded with the help of experimental set-up shown in the figure 5-1. The reflectance spectra of the FBG, before and after the coating, were measured using an OSA with a resolution of 0.2 nm. The output of the OSA light source, i.e. an edge-emitting LED (EELED), was routed to the FBG sensor through a 50:50 single mode optical fiber coupler so that a portion of the light reflected by the FBG sensor can be routed to the input of the OSA. An Excel Visual Basic (VB) Program was developed to record the reflected spectrum from the OSA. The FBG spectra reflected by a Lophine coated FBG is compared with that of a bare FBG in figure 5-2. The bare FBG produced a typical reflectance spectrum with a sharp peak while the coated FBG produced a reflectance spectrum with a much broader peak. In addition, the spectrum produced by the Lophine-coated FBG also shifted to a shorter wavelength. In order to quantify these observed changes, a MATLAB program was developed to extract two spectral parameters, i.e. the central Bragg wavelength and bandwidth, from the measured reflectance spectra. Two wavelengths, i.e. the low cut-off and high cut-off wavelengths, were determined as the wavelengths at which the intensity of the spectrum is 8 dB below the peak intensity. The central Bragg wavelength is then calculated as the average of these two wavelengths while

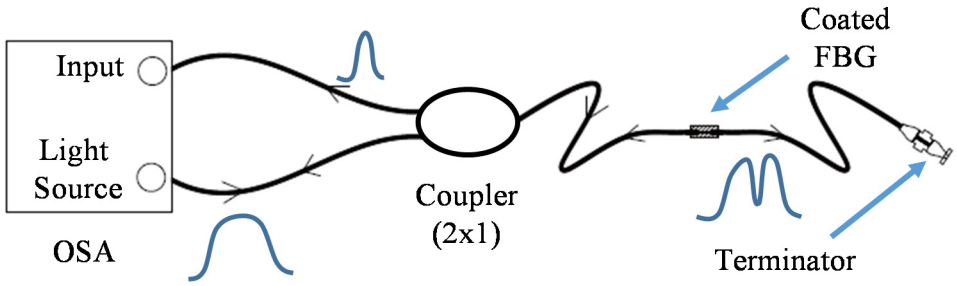

Figure 6-1 Experimental setup for measuring the reflectance spectrum of FBG sensor.

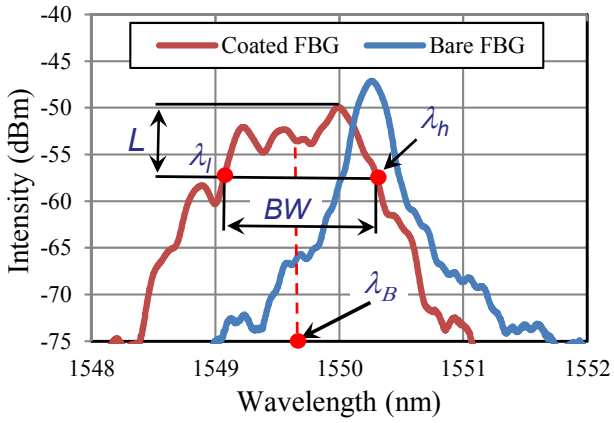

Figure 6-2 Reflectance spectra of the FBG before and after Lophine coating.

the bandwidth is calculated as the difference between these wavelengths and are shown in equation 5-1 and 5-2 respectively. For the bare FBG sensor, the central Bragg wavelength was found to be 1550.255 nm and the bandwidth is 0.447 nm. In contrast, the Lophine-coated FBG has a central wavelength of 1549.567 nm and a bandwidth of 1.561 nm. The shift of the central wavelength toward a shorter wavelength indicated that the coating compresses the FBG. The broadening of the reflectance spectrum is likely due to the non-uniformity of the compressive residual stress introduced by the Lophine coating.

$$\lambda_B = \lambda_h - \lambda_l , \tag{5-1}$$

$$BW = \lambda_h - \lambda_l , \tag{5-2}$$

where λ_B is central Bragg Wavelength, λ_h is high cut-off wavelength, λ_l is Low cut-off wavelength and BW is Bandwidth.

Thermo-Mechanical Testing

The Lophine-coated FBG sensor were tested under simultaneous thermal and mechanical loadings inside a temperature-controllable incubator, as shown in figure 5-3. The optical fiber was hung vertically by gluing its top portion on a flat fixture. The lower

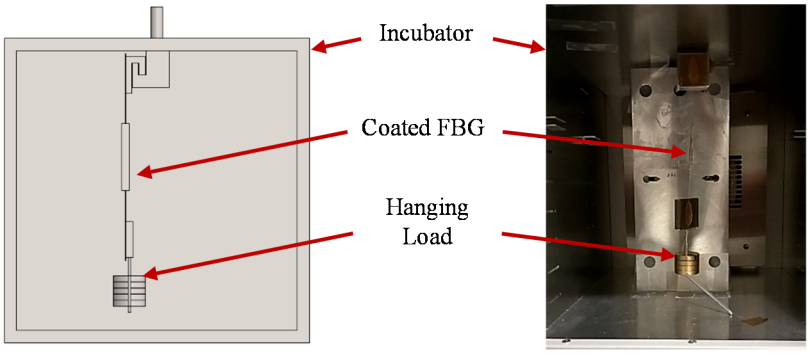

Figure 6-3 Experimental set-up for thermal-mechanical testing of Lophine-coated FBG sensor.

portion of the optical fiber was reinforced with another flat plate so small weights can be hung. The weight was increased from 0 to 80 gm in an increment of 20 gm. Therefore, the axial load experienced by the FBG sensor is the hanging weight plus the weight of the lower flat plate, which is 15.6 gm. Under each weight, the temperature of the incubator was heated from 30 to 60°C in an increment of 5°C. The reflectance spectrum of the FBG sensor was acquired and stored for each weight and temperature combination. The responses of the FBG spectra to the temperature changes, under various different weights, is shown in figure 5-4. For all the cases, the reflectance spectrum shifted to the right while the peak narrowed as temperature was increased.

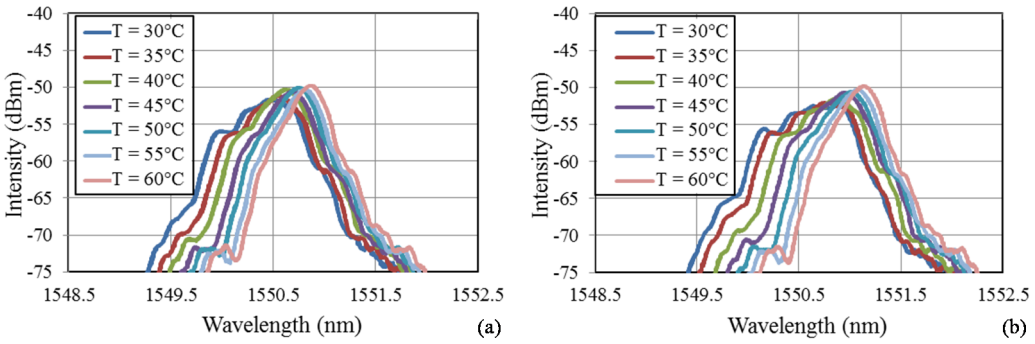

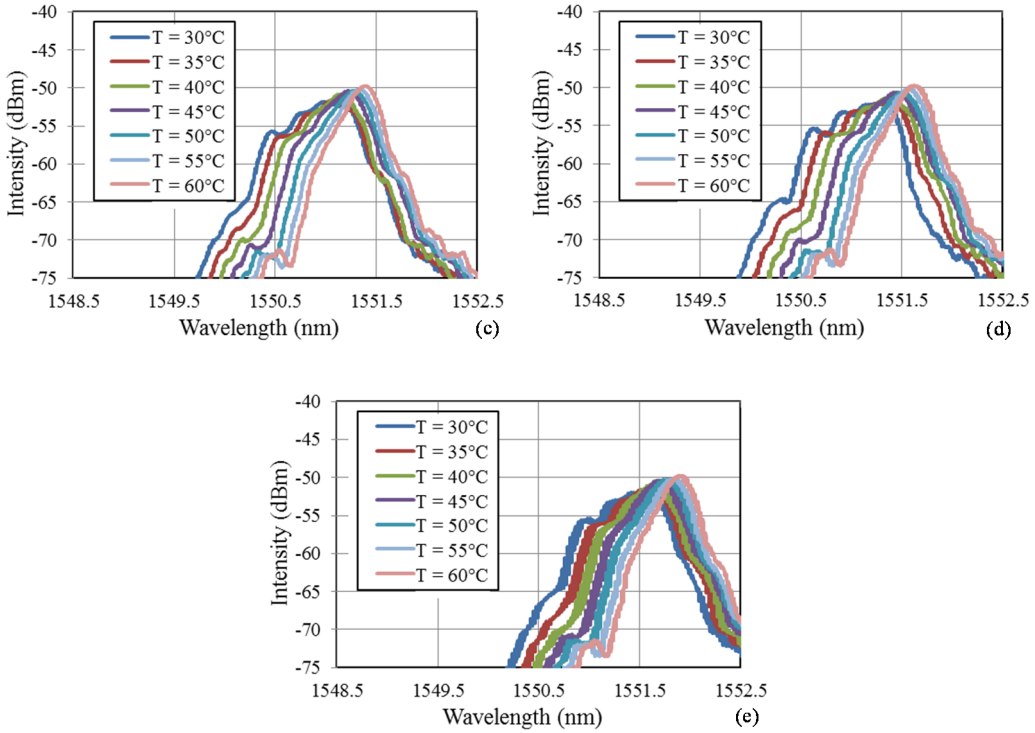

Figure 6-4 Change of FBG spectrum with temperature under two different loads; (a) 0gm; (b) 20gm; (c) 40gm; (d) 60gm; (e) 80gm.

Result

The behavior of spectral parameters are presented against different thermo-mechanical loadings in figure 5-5 and figure 5-6. In figure 5-5, the central Bragg wavelengths and the bandwidths extracted from the reflectance spectra under constant temperatures are plotted versus the axial load. Both the central wavelength (figure 5-5(a)) and the bandwidth (figure 5-5(b)) appear to be linearly proportional to the temperature as well as the axial load. Figure 5-6 shows the central Bragg wavelengths and the bandwidths extracted from the reflectance spectra versus temperature under constant loads. As shown in figure 5-6(a), the central Bragg wavelength increased linearly with increasing

temperature for all loads. The wavelength- temperature curve under different loads are parallel to each other, indicating that the temperature sensitivity, measured as the slope of the wavelength-temperature curve, are similar for all loads. In other words, the applied load seems to affect the intersection of wavelength-temperature curve but not its slope. The bandwidth (figure 5-6(b)) , on the other hand, decreased with increasing temperature but neither the slope nor the intersection of the bandwidth-temperature curve is drastically affected by the applied load.

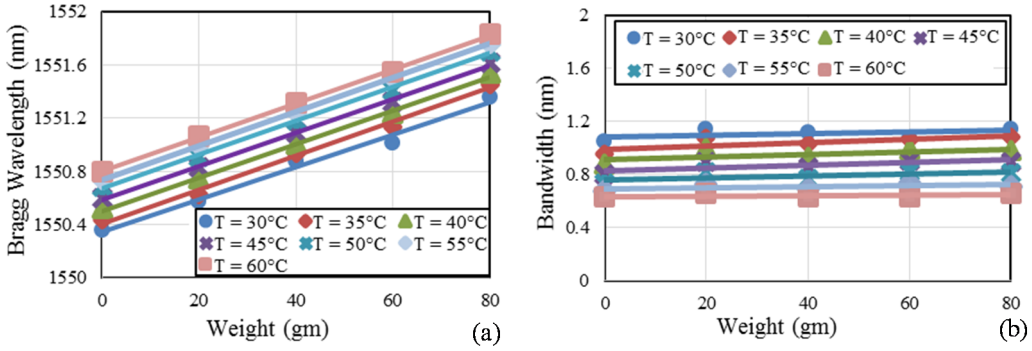

Figure 6-5 The shift in (a) central Bragg wavelength and (b) bandwidth with the applied weight under different temperatures

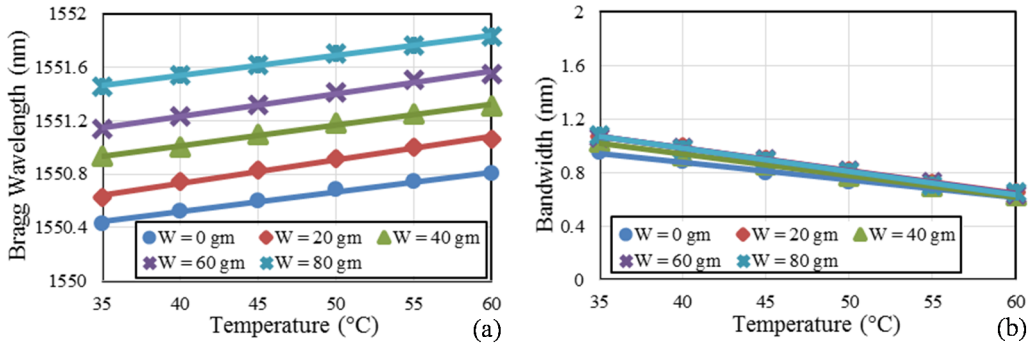

Figure 6-6 The shift in (a) central Bragg wavelength and (b) bandwidth with change in temperature under different weight.

Data Processing

Since both the central wavelength and the bandwidth are the linear functions of temperature (T) as well as axial load (W). Therefore, they can be curve fitted using linear functions, i.e.

$$BW\ (T,W) = -0.01591\ T + 0.00073\ W + 1.559\ , \tag{5-3}$$

$$\lambda_B\ (T,W) = 0.01619\,T + 0.01263\,W + 1550\ , \tag{5-4}$$

where T is the temperature, W is the axial load, BW is the measured bandwidth, and λ_B is the measured Bragg wavelength. The coefficients of linear equations were found using a

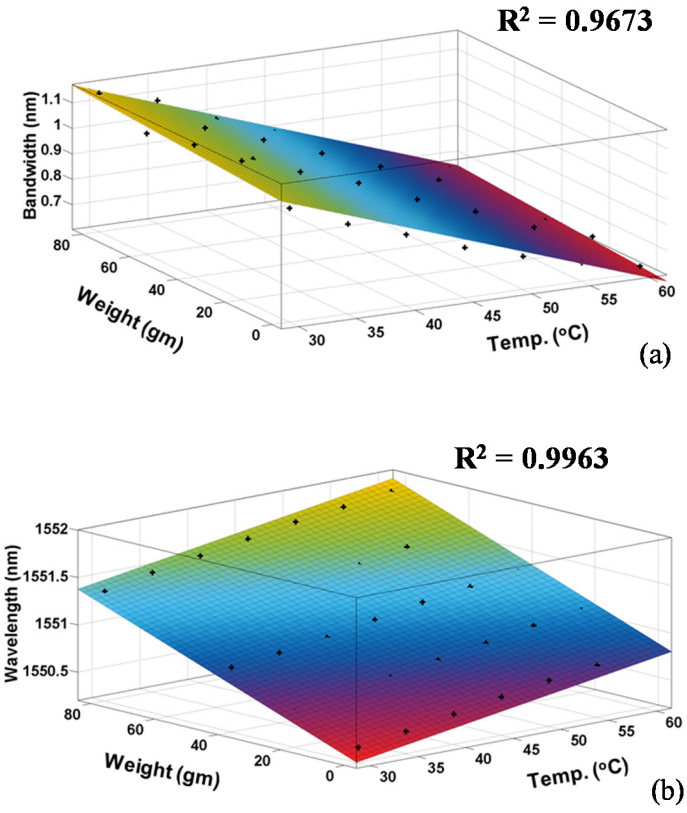

Figure 6-7 Curve fitting for the change in (a) bandwidth and (b) central Bragg wavelength under simultaneous load and temperature varriations.

curve fitting tool available in MATLAB and is shown in figure 5-7. Figure 5-7(a) shows distribution of bandwidth around the fitted curve for temperature and load variations. The result of bandwidth-fit is presented in equation 5-3. A similar approach is adopted to find the fitting-curve for Bragg wavelength and is as shown in figure 5-7 (b). The equation of fitting curve, thus obtained, is presented in equation 5-4.

Error Estimation

Once equations 5-3 and 5-4 are established, the axial load and temperature corresponding to each FBG spectrum can then be inversely determined from the measured FBG bandwidth and Bragg wavelength as

$$\begin{bmatrix} T \\ W \end{bmatrix} = \begin{bmatrix} -0.01591 & 0.00073 \\ 0.01619 & 0.01263 \end{bmatrix}^{-1} \left(\begin{bmatrix} BW \\ \lambda_B \end{bmatrix} - \begin{bmatrix} 1.559 \\ 1550 \end{bmatrix} \right) \begin{pmatrix} ^{\circ}C \\ gm \end{pmatrix}. \quad (5\text{-}5)$$

The differences between the axial load and temperature determined using equation 5-5 and their actual values are presented in figure 5-8. For temperature, the measurement errors are larger at lower temperatures, which are within ± 4 ^{o}C, but the errors reduced to around ± 2 ^{o}C for higher temperatures. On the other hand, the measurement errors for the axial load appear to be independent of the applied load. Except one outlier that produced an error of -9.7 gm, the measurement errors of the axial load are within ± 4 gm. Assume the strain sensitivity of a standard FBG is 1.2 pm/με [9] and the measured load sensitivity of 13.4 pm/gm from our experiment, we estimated that 1 gm of axial load is equivalent to 11.2 με. Therefore, the corresponding strain errors are within ± 44.8 με.

The thermal and mechanical responses of the bare FBG was tested before the coating process and after the Lophine coating was removed. We found that the FBG

responses were repeatable after multiple coating and un-coating processes, which indicated that the molten Lophine does not cause any irreversible effect on the FBG.

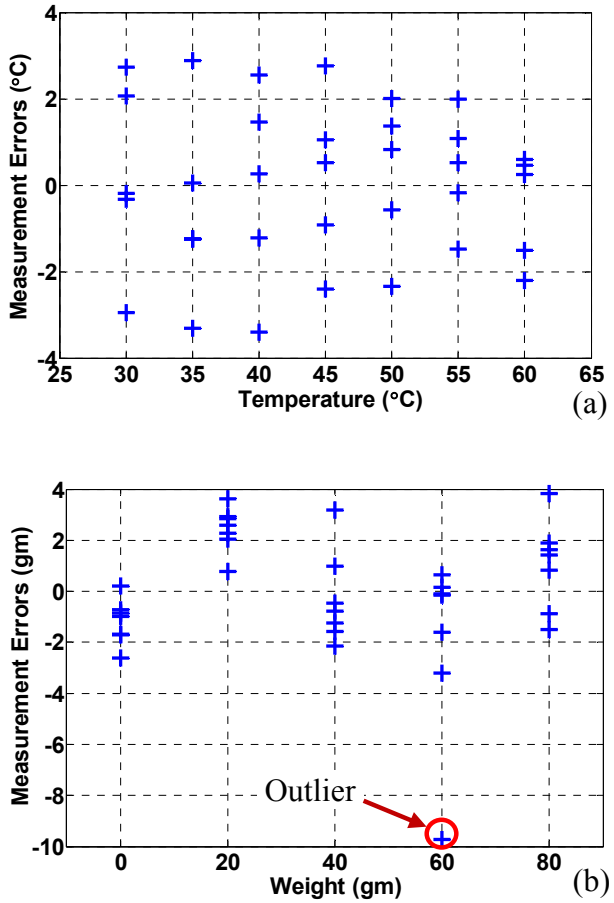

Figure 6-8 Differences between the measurements and the actual values: (a) temperature; (b) applied weight.

Chapter 7

Discussion

The response of coated FBG sensor is promising as it is capable of measuring simultaneous strain and temperature with a high accuracy. The proposed sensor can measure temperature and strain within the error of 4 °C and 44.8 με respectively. Our initial research approach was to introduce bandwidth modulation with the help of a thermochromic coating. However, bandwidth can also be modulated by introducing birefringence or thermal residual stress in the FBG as mentioned by other authors [22,41,42,31]. Now, it becomes essential to investigate the real contributor in bandwidth modulation of our sensor and thus roles of thermochromic coating, Birefringence, and thermal residual stress have been further studied. To validate our principle stand (thermochromic), a Tilted FBG is used whereas the presence of birefringence can be tested by normal FBG sensors.

Thermochromic Effect (TFBG)

Principle of operation

The FBG of proposed sensor is replaced with Tilted FBG (TFBG), also known as blazed FBG. The purpose of TFBG is to have a better interaction between the guided modes and the thermochromic coating by promoting the LP_{01} to LP_{11} mode coupling. As shown in figure 6-1, the mode field of the core mode, typically confined within the fiber core, can be expanded to distribute more optical power into the fiber cladding. As such, the evanescent field of the core mode can interact with the thermochromic coating. Due to the interaction between the enlarged core mode or the LP_{11} cladding mode with the fiber

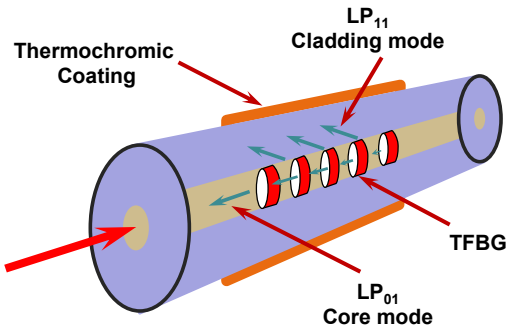

Figure 7-1 Schematic of a tilted FBG sensor that promotes LP_{01}-LP_{11} mode coupling and is coated with the thermochromic material.

coating, the spectral bandwidth of the FBG resonance will be influenced by the optical absorbance of the coating material. Coating the TFBG with a thermochromic material, therefore, will produce temperature dependent bandwidth changes which have higher sensitivity than normal FBG coated with thermochromic material.

It is well established that an FBG will not only introduce the core to core mode coupling (i.e. the LP_{01}- LP_{01} coupling) but also the core to cladding mode coupling (i.e. the LP_{01}- LP_{nl} coupling) [43]. In general, the symmetrical LP_{01} core mode will only couple to the symmetric LP_{01} cladding modes. The coupling from the LP_{01} core mode to the asymmetric LP_{11} cladding mode can be achieved by titling the FBG [44]. As shown in figure 6-2, the

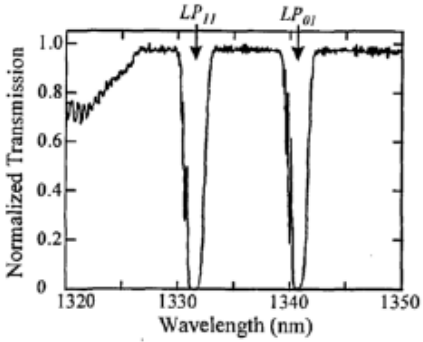

Figure 7-2 Transmission spectrum of a tilted FBG with the LP_{01} and LP_{11} resonances shown and the shorter wavelength cladding modes suppressed [45].

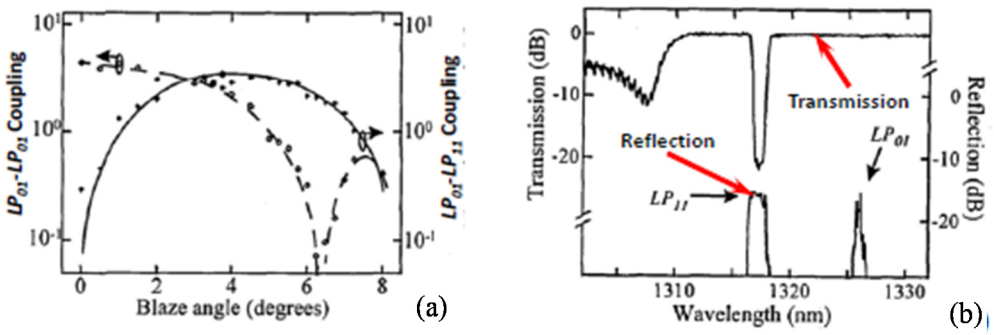

Figure 7-3 Controlling the mode couplings through the tilt angle; (a) coupling strengths of the LP_{01}-LP_{01} and LP_{01}-LP_{11} mode coupling as a function of the FBG tilt angle; b) suppression of the LP_{01}-LP_{01} resonance in the transmission spectrum using an FBG with a tilt angle of 6.1° [45].

transmission spectrum of a typical tilted FBG has two distinct transmission valleys (i.e. resonances) with the LP_{01} resonance corresponds to the LP_{01}-LP_{01} mode coupling and the LP_{11} resonance as a result of the LP_{01}-LP_{11} coupling. The other cladding modes were suppressed by using the cladding depressed fibers [45]. The relative coupling strengths of the LP_{01}-LP_{01} and LP_{01}-LP_{11} mode couplings are functions of the tilt angle, as plotted in figure 6-3(a). At a tilt angle slightly larger than 6°, the LP_{01}-LP_{01} coupling is minimal while the LP_{01}-LP_{11} coupling remains relatively strong. The complete suppression of the LP_{01} resonance in the transmission spectrum of the FBG with a tilt angle of 6.1° is demonstrated in figure 6-3(b). By eliminating the LP_{01} resonance from the FBG transmission spectrum, the TFBG only displayed a single resonance corresponding to the LP_{01}-LP_{11} coupling. Since the LP_{11} mode will have better interaction than LP_{01} mode with the thermochromic coating, the bandwidth of the LP_{11}, transmission resonance, will be affected differently than the bandwidth of the LP_{01}, reflection resonance, for temperature variation only. Therefore, by comparing the thermal dependent bandwidth of core mode (LP_{01}) and cladding mode (LP_{11}) resonance, we can verify the effect of thermochromic material.

Thermal response

The Lophine coated TFBG sensors were fabricated following the procedure mentioned in chapter-4. The experimental set-up for the thermal response of the sensor is presented in figure 6-4. It consists of a broadband light source guided into the core of a SMF, a portion of which is reflected back after its encounter with the TFBG, and is routed to the OSA through a coupler and an optical switch. The transmitted light signal was also sent to the OSA via the same optical switch. The presence of an optical switch provides the flexibility to toggle between the two spectral responses, i.e. reflected and transmitted signal, recorded by the OSA . Sensor was placed in an airtight digital incubator for which the temperature was varied from 30 °C to 60 °C in an interval of 5 °C. Both transmission and reflection spectra of the sensor at each temperature were recorded, with the help of a Visual Basic (VB) Program developed in Excel, and is shown in figure 6-5. The recorded data is then interrogated in the same way as it was done for the normal FBG in chapter-5. The behavior of the core mode in reflection and the cladding mode in transmission, not only displayed similar spectral characteristics, i.e. Bragg wavelength and bandwidth, but were also highly repeatable. We can clearly see a red shift in the Bragg wavelength with increase in temperature while the bandwidth keeps on decreasing. Further, in order to quantify the spectral parameters, and to have a better understanding of their behavior, the

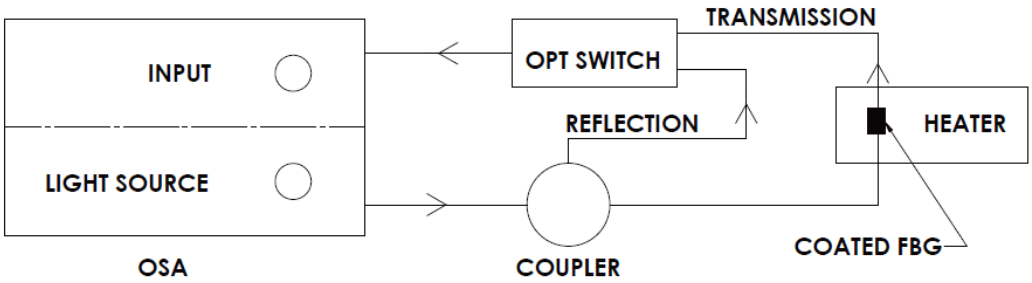

Figure 7-4 Experimental set-up for thermal response of Lophine coated TFBG sensors.

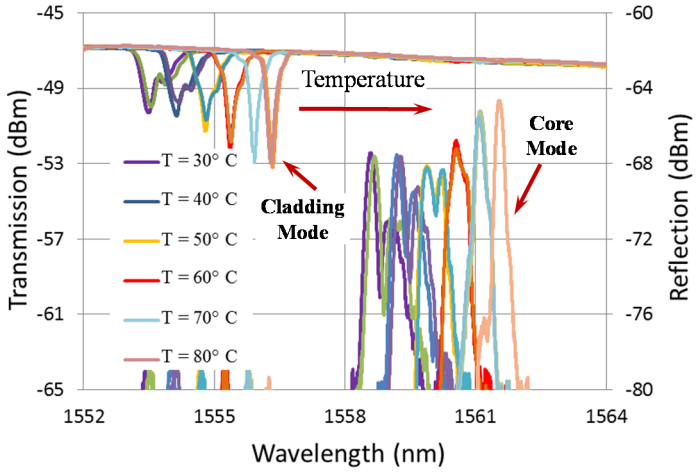

Figure 7-5 Spectral shift of Lophine – coated TFBG sensor.

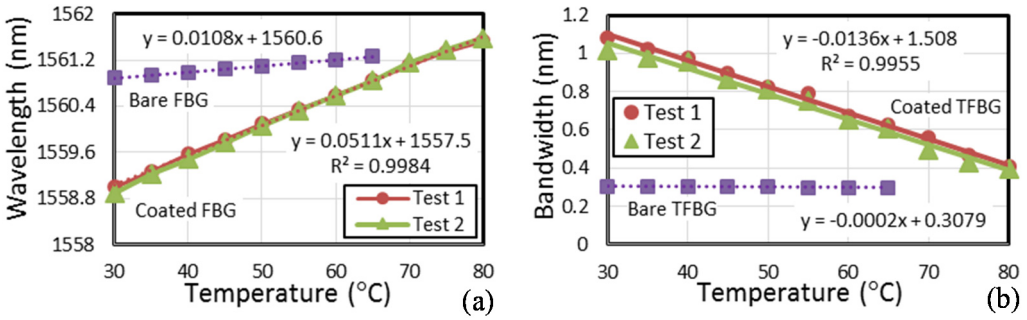

Figure 7-6 Shift in (a) central Bragg wavelength (b) bandwidth with temperature change.

data is processed in MATLAB at a distance of 10 dB from the peak of the reflected signal for which the result is shown in figure 6-6. In figure 6-6(a), central Bragg wavelength of the TFBG sensor, before and after coating, is shown at various temperature. The Bragg wavelength of both the sensors, i.e. Lophine-coated TFBG and bare TFBG, increased linearly with increasing temperature, however the sensitivity of the coated TFBG is found to be nearly five times the bare TFBG sensors (sensitivity of coated TFBG = 51.1 pm/°C and bare TFBG = 10.8 pm/°C). The bandwidth, on the other hand, decreased with increase in temperature for the coated TFBG sensor having a sensitivity of -13.6 pm/°C whereas

the bare TFBG sensor maintain a constant bandwidth at all temperature values, and is shown in figure 6-6(b).

The spectral characteristics of the coated TFBG sensor displayed the result similar to what we have obtained earlier with the coated FBG sensors. With this result, it is difficult to give credit to the thermochromic effect for the bandwidth modulation of the proposed sensor. This motivated us to execute the following experiments:

1. Study the effect of coating thickness
2. Use non-thermochromic material as coating
    a. NOA-61 epoxy
    b. Solder paste

Study the effect of coating thickness

The effect of coating thickness on the bandwidth modulation of TFBG sensor was studied for three different values, i.e. 0.5 mm, 1 mm and 3 mm. Thickness less than 0.5 mm could not be achieved due to fabrication issues. The fabrication process and experimental set-up are the same as used in the previous experiments, and its result is shown in figure 6-7. The sensitivity of bandwidth against temperature change for different thickness is shown in figure 6-7. Irrespective of the coating thickness, we observed a linear decrease in bandwidth with increase in temperature, and the result is highly repeatable. However, as we move from smallest coating thickness to the largest one, two important observation can be made. One, the sensitivity of the bandwidth kept on decreasing with its values -32.3 pm/°C, -18.7 pm/°C and -13.6 pm/°C respectively, and two, the linearity region for the sensor has increased to 60 °C, 65 °C, and 80 °C respectively for the coating thickness of 0.5 mm, 1 mm and 3 mm.

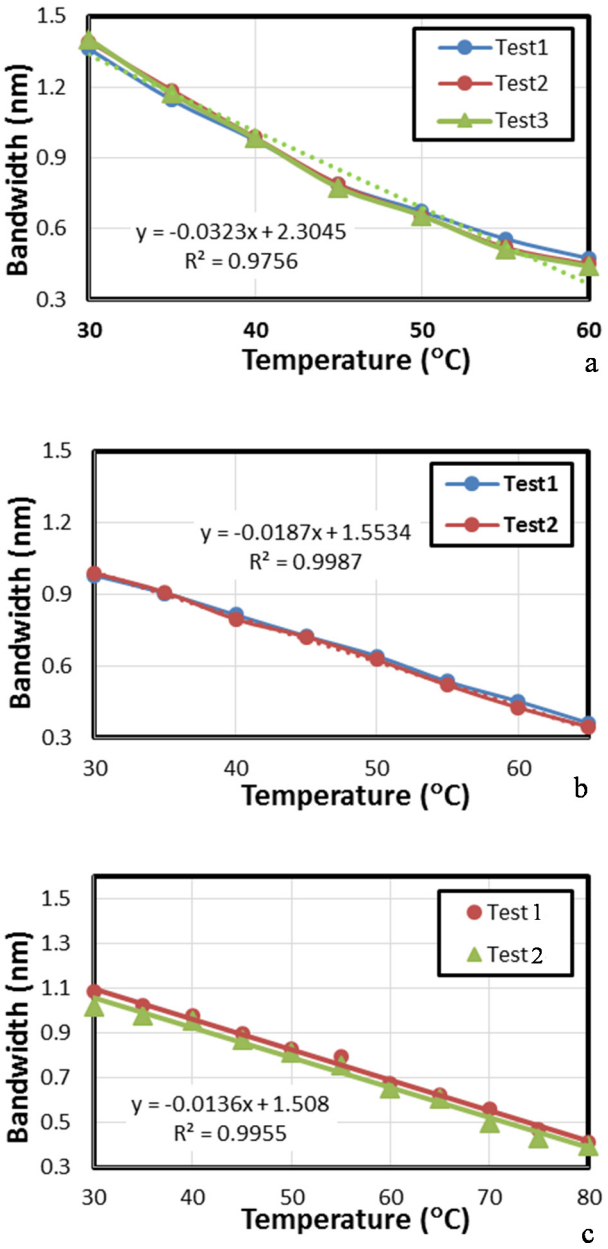

Figure 7-7 Change in bandwidth with temperature for three different thickness of coating;

(a) 0.5 mm, (b) 1 mm and (c) 3 mm.

Use non-thermochromic material as coating

In addition to Lophine, the TFBG sensor was also coated with two different non-thermochromic material, i.e. NOA-61 epoxy and solder paste, and their spectral responses were examined. The coating process for both the materials are already explained in chapter-4. The NOA-61 coated TFBG sensor is shown in figure 6-8(a), and its spectral parameters are characterized for the temperature change in figure 6-9. In figure 6-9(a), central Bragg wavelength is presented both for the core and the cladding mode. Irrespective of the modes, identical results are obtained which varies linearly with changing temperature, and their sensitivity is more than 2.5 times in comparison with the normal TFBG sensors (27 pm/°C > 2.5*10.5 pm/°C). However, we could not achieve bandwidth modulation by using this coating. As shown in the figure 6.9(b), bandwidth of the coated TFBG sensor remained constant at all the temperature values for both the modes.

Solder paste is another non-thermochromic material, coated around TFBG sensor (as shown in figure 6-8(b)), to characterize the modulation of bandwidth as well as Bragg wavelength for which result is shown in figure 6-10. In figure 6-10(a), response of Bragg wavelength is presented both for the core mode and the cladding mode, which can be well divided in two linear regions having different sensitivity, i.e. before 45 °C and after 45 °C.

Figure 7-8 TFBG sensor coated with; (a) NOA-61 epoxy and (b) Solder paste

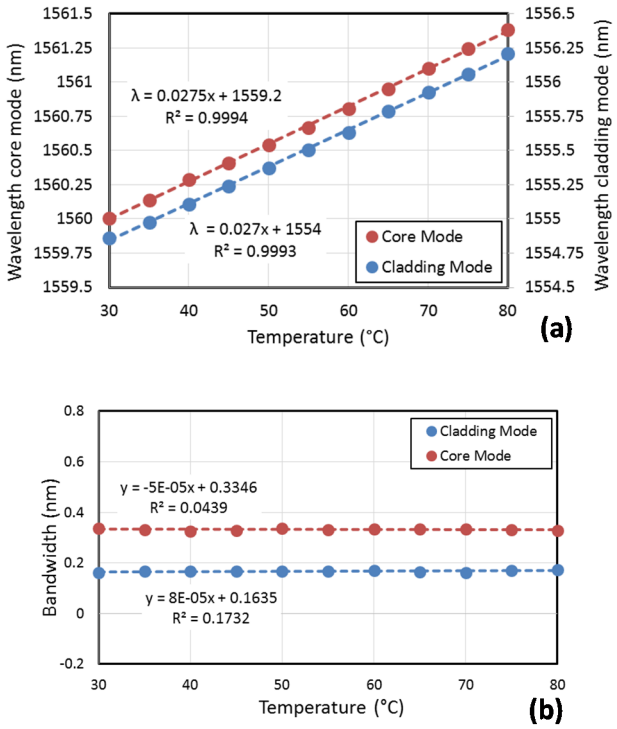

Figure 7-9 Change in (a) Bragg wavelength and (b) bandwidth of NOA-61 coated TFBG sensor versus temperature

It is important to note that both the core and the cladding modes showed similar characteristics. This trend was also continued to the bandwidth response against change in temperature, and is shown in figure 6-10(b). Bandwidth, irrespective of the change in temperature, remained constant throughout experiment and could not be modulated.

Two important observations can be made in this section which is:

1. Neither NOA-61 nor solder paste coating is capable of introducing bandwidth modulation.
2. The thermochromic coating, Lophine, though is able to modulate bandwidth which is consistent with the prediction but the thickness dependent sensitivity of bandwidth suggest the involvement of some other factors.

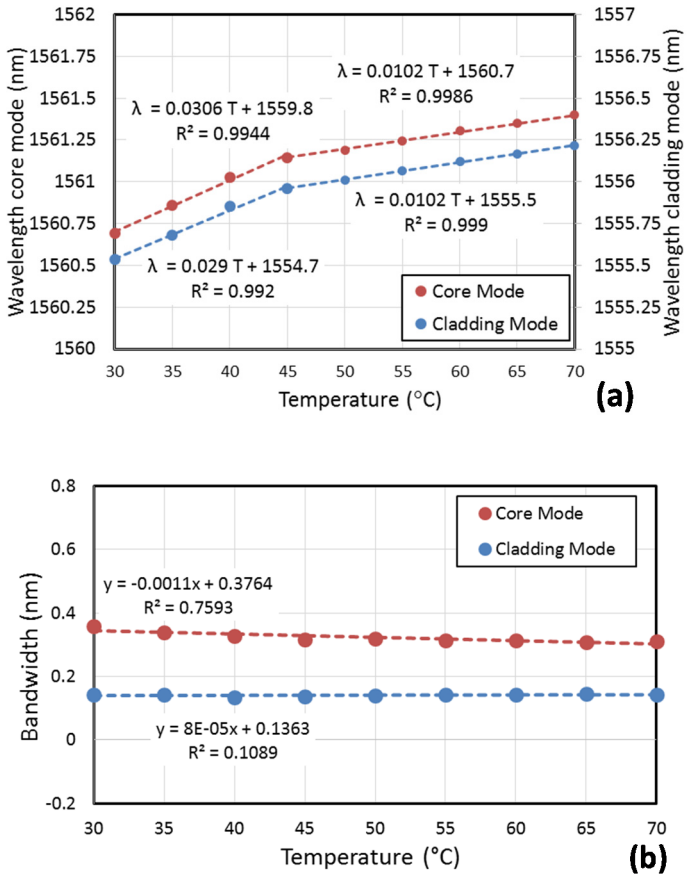

Figure 7-10 Change in (a) Bragg wavelength and (b) bandwidth of TFBG sensor coated with solder paste versus temperature.

Mechanical response

The experimental set-up for the mechanical testing is the same as used in thermal testing except the oven is replaced with mechanical loading mechanism as shown in figure 6-11. One end of the TFBG sensor was glued on a flat plate using adhesive while a weight was hung at the other end and it was increased from 0 to 80 gm in an interval of 10 gm. The reflected spectrum was monitored, recorded, and analyzed in a manner similar to the

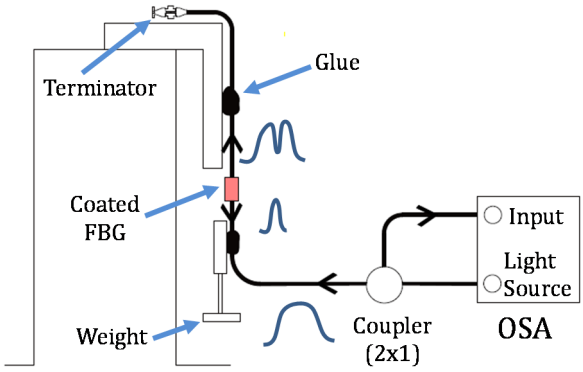

Figure 7-11 Experimental set-up for measuring mechanical-loading response of Lophine coated TFBG sensors.

thermal sensor discussed earlier in this chapter. Figure 6-12 shows the spectral response of Lophine-coated TFBG sensor when exposed to mechanical loading. Since, the cladding mode of the transmitted spectrum follows the same behavior as of the core mode of the reflected spectrum, we have narrowed down our experiment to the study of the core mode only. The spectral response thus obtained were processed, and the result is presented in figure 6-13. In figure 6-13(a), the central Bragg wavelengths of both the bare and the coated FBG sensors are presented which shows a linear red-shift with applied external load. In

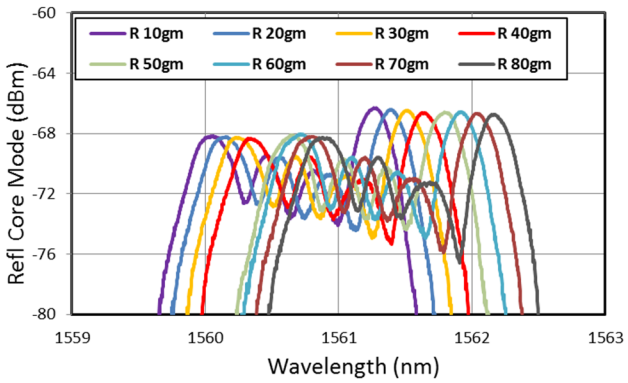

Figure 7-12 Spectral shift of Lophine – coated TFBG sensor with mechanical loading.

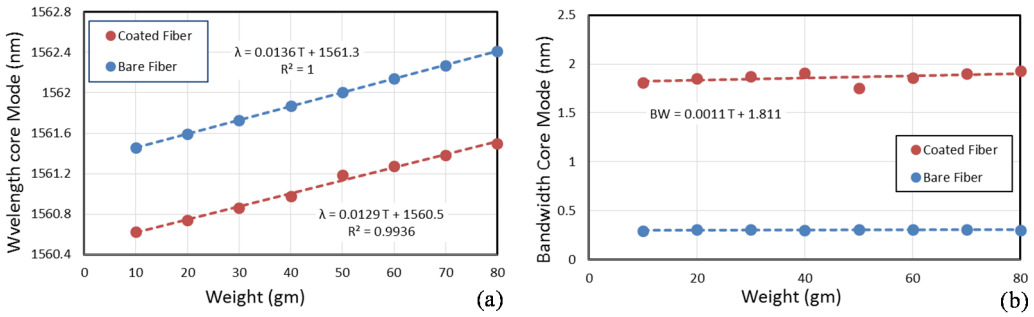

Figure 7-13 Shift in (a) central Bragg wavelength (b) bandwidth with applied mechanical load.

addition, the wavelength sensitivity showed an insignificant difference between the bare and the coated TFBG sensors having their values 13.6 pm/gm and 12.9 pm/gm respectively. However, bandwidth did not show any practical change when exposed to the external loads either for the bare or coated TFBG sensor (figure 6-13(b)).

Birefringence

Principle of operation

The conventional SMF has low birefringence. Thus, when a broadband light travelling in such a fiber encounters an FBG in its path, a narrow band pass spectrum is reflected. Due to its geometric symmetry, the reflected signal contains degenerate Eigen modes and the spectrum carries single resonance peak centered at a wavelength, known as “Bragg wavelength”, λ_b. However, when the same grating is inscribed in a high birefringent fiber, due to the presence of two different Refractive indices, the Eigen modes are no longer degenerate and the reflected spectrum witnesses two resonance peaks, one corresponding to each Eigen value. The resonance peak at shorter wavelength

corresponds to smaller index and is called fast mode, while the one at longer wavelength corresponds to larger RI and is called slow mode.

Birefringence, in traditional SMF, can be developed by distorting its circular symmetry. A common practice is to apply externally – induced stress, confined within a small region. The magnitude of such birefringence is proportional to the stress applied in transverse direction and is shown by equation 6-1.

$$B = n_x - n_y = (n_{x0} - n_{y0}) + C(\sigma_x - \sigma_y)\,, \tag{6-1}$$

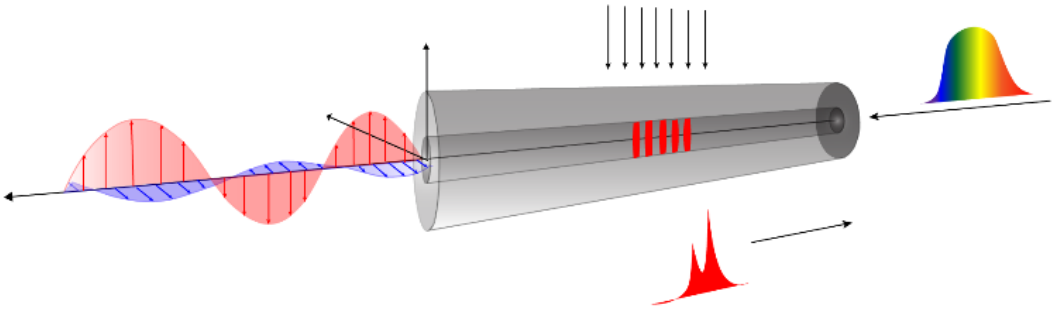

Figure 7-14 Schematic of externally induced birefringence in an FBG sensor and polarization of guided light.

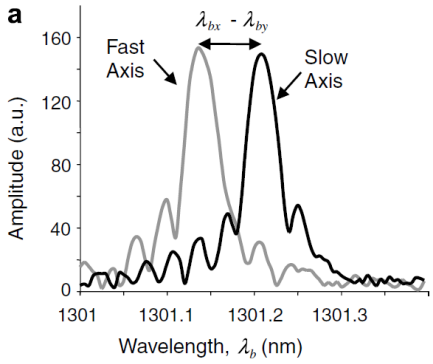

Figure 7-15 Spectral response of the polarized FBG sensor with two axes: fast axis and slow axis [49].

where the first term of birefringence, B, in the expanded form, is the direct result of fiber geometry and arises due to the asymmetry in fiber core [46]. The second term is introduced by stress-induced birefringence, in which 'C' is the stress-optic coefficient whereas 'σ_x' and 'σ_y' represent principal stresses. In case of conventional fiber, effect of first term is negligible and the stress-induced birefringence dominates. Thus, when an FBG is exposed to localized transverse stress (figure 6-14), the uniqueness of Bragg condition no longer exists and the spectrum is characterized by two single peaked spectra centered at two Bragg wavelengths [47] (figure 6-15).and are expressed as:

$$\lambda_{b,s} = 2n_{eff,s}\Lambda, \qquad \lambda_{b,f} = 2n_{eff,f}\Lambda. \tag{6-2}$$

In addition to birefringence, non-uniform strain distribution or thermal residual strain can also produce similar result with splitting of central Bragg wavelength. However, both these effects, i.e. birefringence and residual strain, can be verified using a common experiment. At this moment, we presume birefringence is the sole reason behind such a behavior of FBG sensor having two distinct modes: fast axis and slow axis. If our assumption is correct, the magnitude of reflected intensity of two peaks will change in opposite direction as the polarization of the signal is changed (Figure 6-16). But if the intensity of both reflected peaks vary in the same way, our initial assumption about

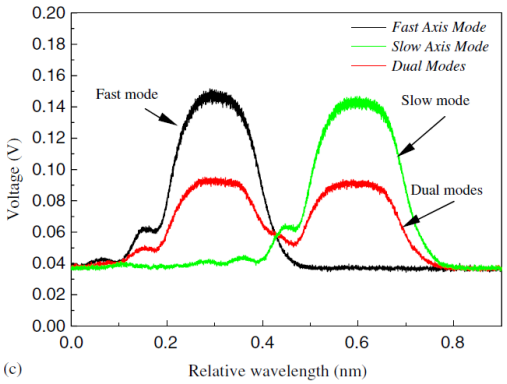

Figure 7-16 Change in FBG spectrum at different polarization state of the signal [31].

birefringence is incorrect and then residual strain can be held accountable for the spectral behavior of the sensor.

Sensor Response

First of all, we have deliberately introduced birefringence in a regular FBG sensor by applying transverse load as shown in the figure 6-17 and have validated the principle using the experimental set-up shown in figure 6-18. Two additional polarization elements, i.e. Polarizer controller (PC) and polarizer filter (PF), were placed in front of an OSA before light is allowed to enter into it. In figure 6-19, the reflected spectrums of the FBG sensors at different angles of polarization (90°, 135° and 180°) were shown for the free and the transversely loaded FBG sensors. As the angle of polarization varied from 0° to 180°, the

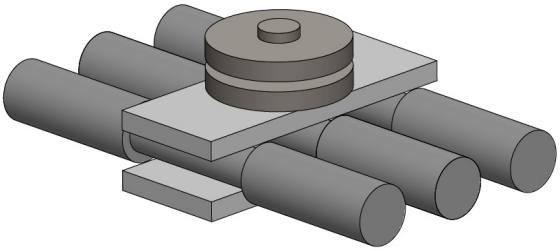

Figure 7-17 Schematics of transversely loaded-FBG sensor for inducing birefringence.

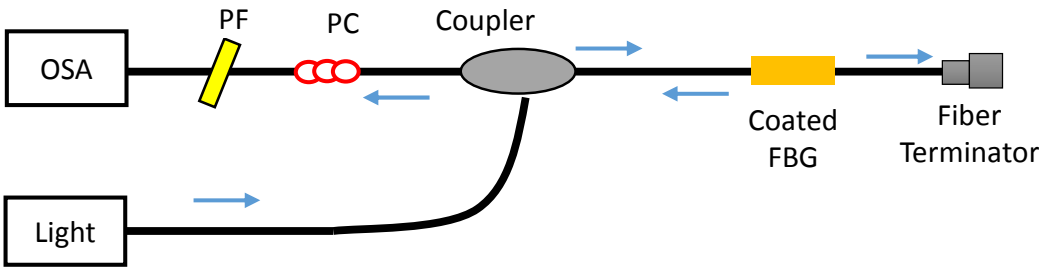

Figure 7-18 Experimental set-up for measuring externally induced birefringence in an FBG sensor (or transversely loaded sensor).

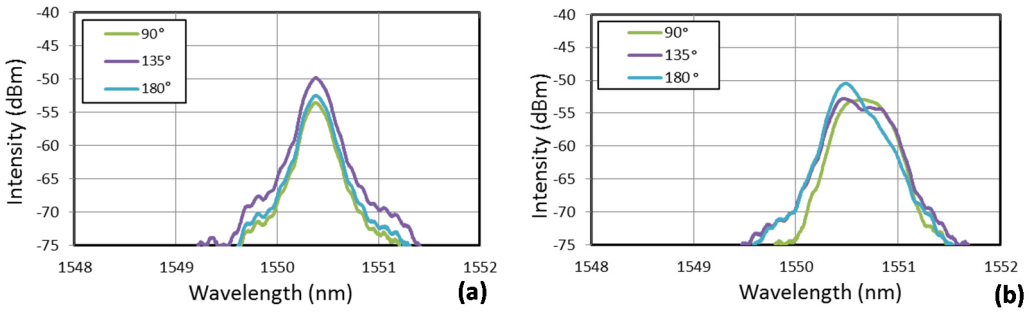

Figure 7-19 Shift in FBG spectrum of (a) normal FBG and (b) transversely-loaded FBG sensor by varying polarization state of the signal.

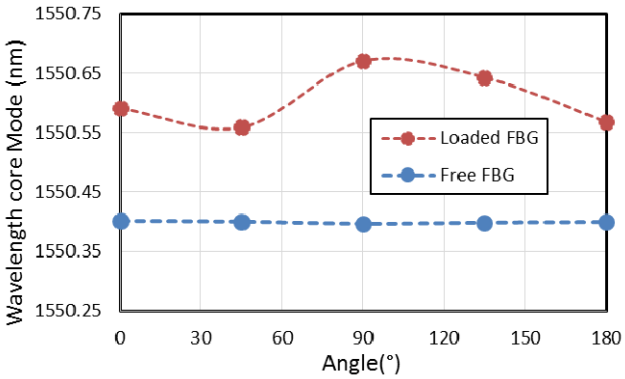

Figure 7-20 Shift in central Bragg wavelength with angle of polarization.

value of central Bragg wavelength kept oscillating for the transversely – loaded FBG sensor while it remained constant for the free FBG sensor, and is shown in figure 6-20. After establishing the relation between the polarized signal and the reflected spectrum of the birefringent FBG sensor, the role of birefringence in the Lophine-coated FBG sensor was investigated, and is shown in figure 6-21. It is clear that irrespective of the polarization of light, the reflected FBG spectrum has constant Bragg wavelength (figure 6-21(a)) and bandwidth (figure 6-21(b)). This violates our initial assumption that the splitting of the peak

is due to birefringence and thus we can claim thermal residual stress for bandwidth modulation of Lophine-coated FBG sensor.

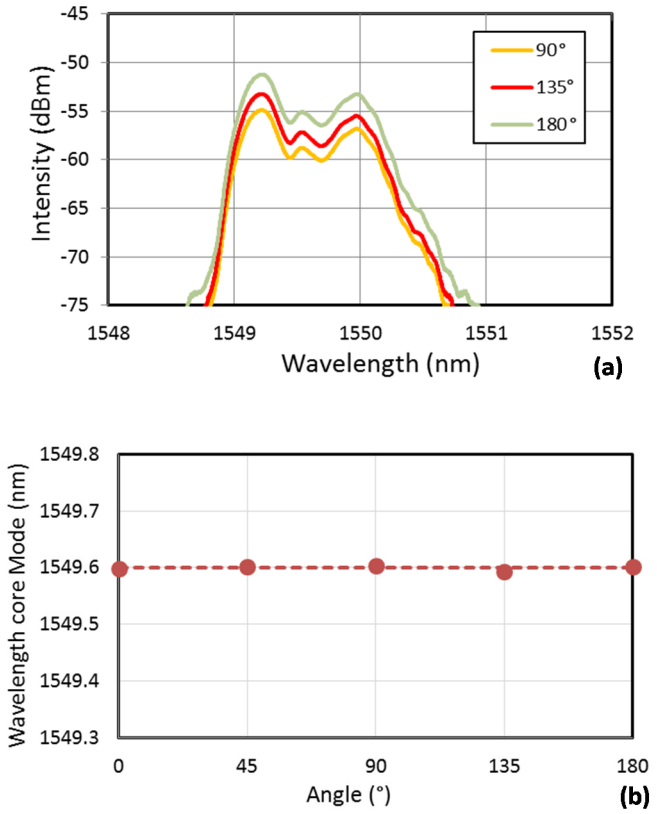

Figure 7-21 (a) Spectrum of Lophine-coated FBG sensor and (b) its central Bragg wavelength at different angle of polarization.

Chapter 8

Conclusion and Future Work

In this research, we demonstrated that coating the FBG sensor with recrystallize Lophine can introduce temperature-dependent bandwidth changes of the FBG reflectance spectrum. Combining the bandwidth change with the central wavelength shift, the axial load and temperature can be simultaneously measured from a single Lophine-coated FBG sensor. The sensor has produced promising result with measurement errors within ±44.8 με for strain and ±4 °C for temperature. Also, Bragg wavelength sensitivity of this sensor against thermal change has increased to 2.5 times normal FBG sensor. On the other hand, the actual reason behind bandwidth modulation could not be validated. Out of the three possible ways, i.e. optical absorption, birefringence and thermal residual stress, it appears that the thermal residual stress developed during the coating process is the reason behind bandwidth modulation of the proposed sensor.

In the future, we will investigate packaging of the Lophine-coated FBG sensor to produce a more robust sensor so that it can be surface mounted on structural components for simultaneous strain and temperature measurements. The other direction worth investigating is the use of composites to embed FBG (figure 7-1). The use of cross ply laminates can introduce birefringence into the FBG and its bandwidth can also be modulated with thermal variation. The advantage of this sensor lies in the fact that it can directly be used for surface mounting application.

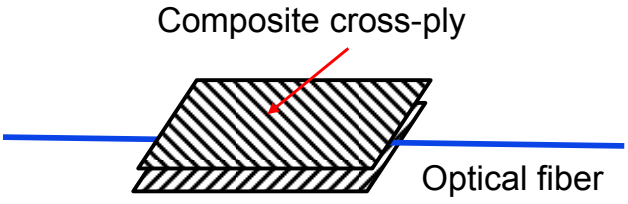

Figure 8-1 FBG embedded in cross ply composite laminate.

Appendix A

MATLAB Code

```
function [WLC, BW]=f_FBG_BW(WL, FBG, BWP);
% this function find the FBG bandwidth at a given power level
% Inputs:
%   WL: wavelength
%   FBG: FBG power
%   BWP: power level at which the BW is calculated
% Output
%   WLC: center wavelength
%   BW: Bandwidth
% First created by Prof. Haiying Huang at Univeristy of Texas Arlington

MM=length(FBG);
plot(WL, FBG,'b', WL, BWP*ones(size(WL)), 'r'); grid on; hold on;

FBG=FBG-BWP;
FBGM=FBG(1:MM-1,1).*FBG(2:MM,1);
WL0=[];

index=find(FBGM==0);  % find data point with zero value
if(~isempty(index))
    index0=find(FBG(index)==0);
    if (~isempty(index0))
        WL0=[WL0; WL(index(index0))];
    end

    index0=find(FBG(index+1)==0);
    if(~isempty(index0))
        WL0=[WL0; WL(index(index0)+1)];
    end
    plot(WL0, BWP(size(WL0)), 'kd');
end

index=find(FBGM<0);  % find zero-crossings
if(~isempty(index))
    WL_Zc=[WL(index), WL(index+1)];
    FBG_Zc=[FBG(index), FBG(index+1)];
    WL0=[WL0;WL_Zc(:,1)-FBG_Zc(:,1).*(WL_Zc(:,2)-WL_Zc(:,1))./(FBG_Zc(:,2)-
FBG_Zc(:,1))];
    plot(WL0, BWP*ones(size(WL0)), 'k*');
end

% if(length(WL0)~=2)
%    disp('warning: more than two intersection, take first & last for BW
calculation');
% end
% WLC=(WL0(2)+WL0(1))/2;
% BW=WL0(2)-WL0(1);
```

```
WLC=(max(WL0)+ min(WL0))/2;
BW= max(WL0)- min(WL0);

return
```

```
% this program process the FBG transmission spectrum to produce the frequency
shift and
% bandwidth changes
clear all
close all
clc
[filename, pathname] = uigetfile({'*.xlsm'},'Open File','Multiselect','off'); %
choose file to open
addpath(pathname); % add path to the matlab search path
FBGT=xlsread(filename, 'Reflection', 't4:ad8195');  %transmission
FBGR=xlsread(filename, 'Reflection', 't4:ad8195');   %reflection
CaseNum=[1:10]; %[num, Case, raw]=xlsread(filename, 'Air', 'E2:H2');
rmpath(pathname); % remove path

[MM, NN]=size(FBGT);
WL=FBGT(:,1);
figure(5); subplot(2,1,1); plot(WL, FBGT(:,2:NN));title('Transmission');grid on;
subplot(2,1,2); plot(WL, FBGR(:, 2:NN));title('Reflection');grid on;

%process resonance
proceed=input('process resonant (Y/N)? ', 's');
kk=0;
figure(10);
while(proceed=='Y')
    clf(10);
    kk=kk+1;
    WLstart=input('Starting wavelength: ');
    WLend=input('Ending wavelength: ');
    index=find(WL>=WLstart & WL<=WLend);
    WL1=WL(index);
    FBG1=FBGT(index, 2:NN);
    FBG2=FBGR(index, 2:NN);
    figure(10); plot(WL1, FBG1);grid on; title('Transmission');
    BW_offsetT=input('Offset from min for BW measurement - Transmission (enter 0
if no resonance): ');
    plot(WL1, FBG2);grid on; title('Reflection');
    BW_offsetR=input('Offset from min for BW measurement - Reflection (enter 0 if
no resonance): ');

    for ii=1:NN-1
        if (BW_offsetT==0)  % no obvious peak
```

```
            WL_T(ii,kk)=(WLstart+WLend)/2;
            BW_T(ii,kk)=0;
        else
            [WL_T(ii, kk), BW_T(ii, kk)]=f_FBG_BW(WL1, FBG1(:,ii),
min(FBG1(:,ii))+BW_offsetT);
        end

        if (BW_offsetR==0)  % no obvious peak
            WL_R(ii,kk)=(WLstart+WLend)/2;
            BW_R(ii,kk)=0;
        else
            [WL_R(ii, kk), BW_R(ii, kk)]=f_FBG_BW(WL1, FBG2(:,ii),
max(FBG2(:,ii))-BW_offsetR);
        end
    end

    proceed=input('process resonant (Y/N)? ', 's');
end

figure(20);
subplot(2,2,1); plot(CaseNum, WL_T); title('Wavelength shift-Transmission');
xlabel('Case'); ylabel('Wavelength (nm)');
subplot(2,2,2); plot(CaseNum, BW_T); title('FBG BW-Transmission'); xlabel('Case');
ylabel('Wavelength (nm)');
subplot(2,2,3); plot(CaseNum, WL_R); title('Wavelength shift-Reflection');
xlabel('Case'); ylabel('Wavelength (nm)');
subplot(2,2,4); plot(CaseNum, BW_R); title('FBG BW-Reflection'); xlabel('Case');
ylabel('Wavelength (nm)');

% print the output
fid=fopen('FBG_WL_BW.txt', 'w');

for jj=1:kk  % loop over number of resonance
    fprintf(fid, '%s\n', ['Resonant No. ', num2str(jj)]);
    fprintf(fid, '%s \t %s \t %s \t %s \t %s \n','Case', 'Transmission-Freq.',
'Transmission-BW', 'Reflection-Freq.', 'Reflection-BW');
    fprintf(fid, '%10.4f \t %10.4f \t %10.4f \t %10.4f \t %10.4f\n', [CaseNum.',
WL_T(:,jj), BW_T(:,jj), WL_R(:,jj), BW_R(:,jj)].');
end
fclose(fid);
type FBG_WL_BW.txt; % displace the output data
```

References

[1] Lopez-Higuera J M, Rodriguez Cobo L, Quintela Incera A and Cobo A 2011 Fiber Optic Sensors in Structural Health Monitoring *J. Light. Technol.* **29** 587–608

[2] Chan T H T, Yu L, Tam H Y, Ni Y Q, Liu S Y, Chung W H and Cheng L K 2006 Fiber Bragg grating sensors for structural health monitoring of Tsing Ma bridge: Background and experimental observation *Eng. Struct.* **28** 648–59

[3] Guo H, Xiao G, Mrad N and Yao J 2011 Fiber optic sensors for structural health monitoring of air platforms *Sensors* **11** 3687–705

[4] Kahandawa G C, Epaarachchi J, Wang H and Lau K T 2012 Use of FBG sensors for SHM in aerospace structures *Photonic Sensors* **2** 203–14

[5] Majumder M, Gangopadhyay T K, Chakraborty A K, Dasgupta K and Bhattacharya D K 2008 Fibre Bragg gratings in structural health monitoring-Present status and applications *Sensors Actuators, A Phys.* **147** 150–64

[6] TODD M D, NICHOLS J M, TRICKEY S T, SEAVER M, NICHOLS C J and VIRGIN L N 2006 Bragg grating-based fibre optic sensors in structural health monitoring *Philos. Trans. R. Soc. A* **365** 317–43

[7] Mahakud R, Kumar J, Prakash O and Dixit S K 2013 Study of the nonuniform behavior of temperature sensitivity in bare and embedded fiber Bragg gratings: experimental results and analysis. *Appl. Opt.* **52** 7570–9

[8] Alemohammad H and Toyserkani E 2009 Simultaneous measurement of temperature and tensile loading using superstructure FBGs developed by laser direct writing of periodic on-fiber metallic films *Smart Mater. Struct.* **18** 95048

[9] Rao Y J 1997 In-fibre Bragg grating sensors *Meas. Sci. Technol.* **8** 355–75

[10] Baldwin C S, Poloso T, Chen P C, Niemczuk J B, Kiddy J S and Ealy C 2001 Structural monitoring of composite marine piles using fiber optic sensors *SPIE's 8th*

Annu. Int. Symp. Smart Struct. Mater. **4330** 487–97

[11] Rao Y J 2006 Recent progress in fiber-optic extrinsic Fabry-Perot interferometric sensors *Opt. Fiber Technol.* **12** 227–37

[12] Abi Kaed Bey S K, Sun T and Grattan K T V 2008 Simultaneous measurement of temperature and strain with long period grating pairs using low resolution detection *Sensors Actuators A Phys.* **144** 83–9

[13] Triollet S, Robert L, Marin E and Ouerdane Y 2011 Discriminated measures of strain and temperature in metallic specimen with embedded superimposed long and short fibre Bragg gratings *Meas. Sci. Technol.* **22** 15202

[14] Xiaohong L, Dexiang W, Fujun Z and Enguang D 2004 Simultaneous independent temperature and strain measurement using one fiber Bragg grating based on the etching technique *Microw. Opt. Technol. Lett.* **43** 478–81

[15] Dong Y, Chen L and Bao X 2010 High-Spatial-Resolution Time-Domain Simultaneous Strain and Temperature Sensor Using Brillouin Scattering and Birefringence in a Polarization-Maintaining Fiber *Photonics Technol. Lett. IEEE* **22** 1364–6

[16] Cavaleiro P M, Arajo F M, Ferreira L A, Santos J L and Farahi F 1999 Simultaneous measurement of strain and temperature using Bragg gratings written in germanosilicate and boron codoped germanosilicate fibers *IEEE Phot. Technol. Lett.* **11** 1635–7

[17] Dong X, Liu Y, Liu Z and Dong X 2001 Simultaneous displacement and temperature measurement with cantilever-based fiber Bragg grating sensor *Opt. Commun.* **192** 213–7

[18] Jin L, Zhang W, Zhang H, Liu B, Zhao J, Tu Q, Kai G and Dong X 2006 An embedded FBG sensor for simultaneous measurement of stress and temperature

IEEE Photonics Technol. Lett. **18** 154–6

[19] Zhang W, Dong X, Zhao Q, Kai G and Yuan S 2001 FBG-type sensor for simultaneous measurement of force (or displacement) and temperature based on bilateral cantilever beam *IEEE Photonics Technol. Lett.* **13** 1340–2

[20] Dennison C R and Wild P M 2012 Superstructured fiber-optic contact force sensor with minimal cosensitivity to temperature and axial strain *Appl. Opt.* **51** 1188

[21] Sheng H-J and Tien C-L 2006 High-sensitivity simultaneous pressure and temperature sensor using a superstructure fiber grating *IEEE Sens. J.* **6** 691–6

[22] Okabe Y, Yashiro S, Tsuji R, Mizutani T and Takeda N 2002 Effect of thermal residual stress on the reflection spectrum from fiber Bragg grating sensors embedded in CFRP laminates *Compos. - Part A Appl. Sci. Manuf.* **33** 991–9

[23] Tanaka N, Okabe Y and Takeda N 2003 Temperature-compensated strain measurement using fiber Bragg grating sensors embedded in composite laminates *Smart Mater. Struct.* **12** 940–6

[24] Guo T, Zhao Q, Zhang H, Xue L, Li G, Dong B, Liu B, Zhang W, Kai G and Dong X 2006 Temperature-insensitive fiber Bragg grating force sensor via a bandwidth modulation and optical-power detection technique *J. Light. Technol.* **24** 3797–802

[25] Ng J H, Zhou X, Yang X and Hao J 2007 A simple temperature-insensitive fiber Bragg grating displacement sensor *Opt. Commun.* **273** 398–401

[26] Kim S, Kwon J, Kim S and Lee B 2000 Temperature-independent strain sensor using a chirped grating partially embedded in a glass tube *IEEE Photonics Technol. Lett.* **12** 678–80

[27] Xu M G, Dong L, Reekie L, Tucknott J A and Cruz J L 1995 Temperature-independent strain sensor using a chirped Bragg grating in a tapered optical fibre *Electron. Lett.* **31** 823–5

[28] Hadjifotiou T 2008 The Cable and Telecommunications Professional's Reference *Physics* ed H Goff pp 111–44

[29] Othonos A and Introduction I 1997 Fiber Bragg gratings *Rev. Sci. Instrum.* **68** 4309–41

[30] Zervas M N, Ibsen M and Laming R I 1997 Short-wavelength transmission-loss suppression in fibre Bragg gratings 39–41

[31] Lee J R, Tsuda H and Koo B Y 2007 Single-mode fibre optic Bragg grating sensing on the base of birefringence in surface-mounting and embedding applications *Opt. Laser Technol.* **39** 157–64

[32] Kiri P, Warwick M E A, Ridley I and Binions R 2011 Fluorine doped vanadium dioxide thin films for smart windows *Thin Solid Films* **520** 1363–6

[33] Karlessi T, Santamouris M, Apostolakis K, Synnefa A and Livada I 2009 Development and testing of thermochromic coatings for buildings and urban structures *Sol. Energy* **83** 538–51

[34] Qian G and Wang Z Y 2012 Near-infrared thermochromic diazapentalene dyes *Adv. Mater.* **24** 1582–8

[35] Xu G, Huang C M, Tazawa M, Jin P, Chen D M and Miao L 2008 Electron injection assisted phase transition in a nano-Au-VO2 junction *Appl. Phys. Lett.* **93** 96–9

[36] Fernández-Valdivielso C, Matías I R and Arregui F J 2002 Simultaneous measurement of strain and temperature using a fiber Bragg grating and a thermochromic material *Sensors Actuators A Phys.* **101** 107–16

[37] Díaz-Herrera N, Navarrete M C, Esteban O and González-Cano A 2004 A fibre-optic temperature sensor based on the deposition of a thermochromic material on an adiabatic taper *Meas. Sci. Technol.* **15** 353–8

[38] Fernández-Valdivielso C, Egozkue E, Matías I R, Arregui F J and Bariáin C 2003

Experimental study of a thermochromic material based optical fiber sensor for monitoring the temperature of the water in several applications *Sensors Actuators B Chem.* **91** 231–40

[39] Yoo W J, Seo J K, Jang K W, Heo J Y, Moon J S, Park J Y, Park B G and Lee B 2011 Fabrication and comparison of thermochromic material-based fiber-optic sensors for monitoring the temperature of water *Opt. Rev.* **18** 144–8

[40] Loh W H, Cole M J, Zervas M N, Barcelos S and Laming R I 1995 Complex grating structures with uniform phase masks based on the moving fiber-scanning beam technique. *Opt. Lett.* **20** 2051–3

[41] Kuang K S C, Kenny R, Whelan M P, Cantwell W J and Chalker P R 2001 Embedded fibre Bragg grating sensors in advanced composite materials *Compos. Sci. Technol.* **61** 1379–87

[42] Kuang K S C, Kenny R, Whelan M P, Cantwell W J and Chalker P R 2001 Residual strain measurement and impact response of optical fibre Bragg grating sensors in fibre metal laminates *Smart Mater. Struct.* **10** 338–46

[43] Erdogan T 1997 Fiber grating spectra *J. Light. Technol.* **15** 1277–94

[44] Dong X, Zhang H, Liu B and Miao Y 2011 Tilted fiber bragg gratings: Principle and sensing applications *Photonic Sensors* **1** 6–30

[45] Strasser T A, Pedrazzani J R and Andrejco M J 1997 Reflective-mode conversion with UV-induced phase gratings in two-mode fiber *Proc. Conf. Opt. Fiber Communation* 348–9

[46] Okamoto K, Hosaka T and Edahiro T 1981 Stress analysis of optical fibers by a finite element method *IEEE J. Quantum Electron.* **17** 2123–9

[47] Chen G C G, Liu L L L, Jia H J H, Yu J Y J, Xu L X L and Wang W W W 2004 Simultaneous strain and temperature measurements with fiber Bragg grating

written in novel Hi-Bi optical fiber *IEEE Photonics Technol. Lett.* **16** 221–223

[48] Newport Fiber Optic Basics

[49] Sorensen L, Botsis J, Gmür T and Cugnoni J 2007 Delamination detection and characterisation of bridging tractions using long FBG optical sensors *Compos. Part A Appl. Sci. Manuf.* **38** 2087–96

Biographical Information

Mr. Abhay was born in Bihar, India in 1990. He obtained his bachelor's degree in Mechanical engineering from Panjab University, Chandigarh, in 2013. Thereafter, he joined the design and research team of Oceaneering, an oil and gas industry. In 2014, he decided to pursue further education by joining The University of Texas at Arlington as a graduate research assistant. His research lies in the field of structural health monitoring. He primarily designs optical fiber sensors for simultaneous measurement of temperature and strain. His research work was published in *Smart Materials and Structures* journal of IOP and in *SMASIS* conference of American Society of Mechanical Engineer (ASME) before his graduation in 2016. He is a recipient of multiple awards and honors such as *travel grant award* from University of Texas at Arlington, *Tau Beta Pi* recognition for academic excellence and *ASME* membership. He is also certified as professional design engineer, a certificate issued by *Dassault Systèmes*. Among other extracurricular activities, he served as an executive member and social liaison of ASME UT Arlington chapter.